Author/s:
Yoh, HZ;Chen, Y;Aslanoglou, S;Wong, S;Trifunovic, Z;Crawford, S;Lestrell, E;Priest, C;Alba, M;Thissen, H;Voelcker, NH;Elnathan, R

Title:
Polymeric Nanoneedle Arrays Mediate Stiffness-Independent Intracellular Delivery

Date:
2022-01-01

Citation:
Yoh, H. Z., Chen, Y., Aslanoglou, S., Wong, S., Trifunovic, Z., Crawford, S., Lestrell, E., Priest, C., Alba, M., Thissen, H., Voelcker, N. H. & Elnathan, R. (2022). Polymeric Nanoneedle Arrays Mediate Stiffness-Independent Intracellular Delivery. Advanced Functional Materials, 32 (3), https://doi.org/10.1002/adfm.202104828.

Polymeric nanoneedle arrays mediate stiffness-independent intracellular delivery

Hao Zhe Yoh,[#] Yaping Chen,[#] Stella Aslanoglou, Sherman Wong, Zlatan Trifunovic, Simon Crawford, Esther Lestrell, Craig Priest, Maria Alba, Helmut Thissen, Nicolas H. Voelcker,* Roey Elnathan**

H. Yoh, Dr. Y. Chen, S. Aslanoglou, E. Lestrell, Dr. M. Alba, Prof. N. H. Voelcker, Dr. R. Elnathan
Monash Institute of Pharmaceutical Sciences
Monash University
381 Royal Parade, Parkville, VIC 3052, Australia
E-mail: crystal.chen@monash.edu; nicolas.voelcker@monash.edu; roey.elnathan@monash.edu

H. Yoh, Dr. Y. Chen, S. Aslanoglou, E. Lestrell, Dr. M. Alba, Prof. N. H. Voelcker, Dr. R. Elnathan
Melbourne Centre for Nanofabrication
Victorian Node of the Australian National Fabrication Facility
151 Wellington Road, Clayton, VIC 3168, Australia

H. Yoh, E. Lestrell, Dr. M. Alba, Dr. H. Thissen, Prof. N. H. Voelcker
Commonwealth Scientific and Industrial Research Organization (CSIRO)
Clayton, VIC 3168, Australia

Prof. N. H. Voelcker, Dr. R. Elnathan
Department of Materials Science and Engineering, Monash University, 22 Alliance Lane, Clayton, VIC 3168, Australia.

Prof. N. H. Voelcker
INM-Leibnitz Institute for New Materials, Campus D2 2, Saarbrücken 66123, Germany.

A/Prof. C. Priest
Future Industries Institute, UniSA STEM, University of South Australia, Mawson Lakes, SA, 5095 Australia

A/Prof. C. Priest
Australian National Fabrication Facility, South Australia Node, University of South Australia, Mawson Lakes, SA, 5095 Australia

Dr. S. Wong
Physics, School of Science, RMIT University, Melbourne, VIC 3000, Australia

Z. Trifunovic

This is the author manuscript accepted for publication and has undergone full peer review but has not been through the copyediting, typesetting, pagination and proofreading process, which may lead to differences between this version and the Version of Record. Please cite this article as doi: 10.1002/adfm.202104828.

Ian Holmes Imaging Centre
Bio21 Molecular Science and Biotechnology Institute
The University of Melbourne, VIC 3010, Australia

S. Crawford
Ramaciotti Centre for Cryo Electron Microscopy,
Monash University, VIC 3800, Australia

Keywords: polymeric nanoneedles, cell–nanoneedle interfaces, membrane deformations, intracellular delivery, mRNA transfection, endocytic pits

Abstract

Tunable vertically aligned nanostructures, usually fabricated using inorganic materials, are powerful nanoscale tools for advanced cellular manipulation. But nanoscale precision typically requires advanced nanofabrication machinery and involves high manufacturing costs. By contrast, polymeric nanoneedles (NNs) of precise geometry can be produced by replica molding or nanoimprint lithography—both rapid, simple, and cost-effective. Polymeric NNs have the additional benefits of flexibility and optical transparency. Here, we engineer cytocompatible polymeric arrays of NNs with identical topographies but differing stiffness, using polystyrene (PS), SU8, and polydimethylsiloxane (PDMS). By interfacing the polymeric NN arrays with adherent and suspension mammalian cells, and comparing the cellular responses of each of the three polymeric substrates, we decouple the influence of substrate stiffness from topography on cell behavior. Notably, we demonstrate the ability of PS, SU8, and PDMS NNs to facilitate mRNA delivery to GPE86 cells with 26.8±3.5%, 33.2±7.4%, and 30.1±4.1% average transfection efficiencies respectively. Electron microscopy reveals the intricacy of the cell–NN interactions; and immunofluorescence imaging demonstrates that enhanced endocytosis is one of the mechanisms of PS NN-mediated intracellular delivery, involving the endocytic proteins caveolin-1 and clathrin heavy chain. Our results provide insights into the interfacial interactions between cells and polymeric NNs, and their related intracellular delivery mechanisms.

1. Introduction

There has been significant progress in the field of engineered nano–bio cellular interfaces.[1] In particular, vertically aligned NNs—such as porous and non-porous nanowires,[2] nanostraws,[3] and nanotubes,[4] and their electroactive analogues[5]—have been interfaced with biological systems to partially control and probe cell function, behavior, and fate.[6] The advantages of NNs include their capacity for: (i) tight interface with cells, negotiating local biological barriers with minimal invasiveness and perturbation;[7] (ii) geometric/architectural flexibility and tunable physical properties;[8] and (iii) simultaneous interactions with a large number of cells in culture, or at the surface of a tissue.[9] Such diverse and tunable NNs are now being exploited for increasingly complex cellular manipulation, such as intracellular delivery,[10] *in vivo* and *ex vivo* gene editing,[9, 10d, 11] biomolecular extraction/sampling,[12] intracellular probing of action potentials,[13] immunomodulation,[14] biosensing,[15] and mechanotransduction.[2a, 16]

Despite NN implementation in advanced cellular/tissue applications, mechanisms behind the biological responses to engineered cell–NN interfaces remain elusive.[1a,1b,17] Through various manufacturing approaches, NNs can differ greatly in their fabrication complexity and patterning,[18] and their physico-chemical properties such as chemical composition, topography, rigidity, porosity, and opacity[19]. All of these factors further complicate attempts to understand their interfacial interactions with biological systems. For instance, the opaqueness of silicon (Si) substrates can restrict characterization and evaluation of dynamic cellular processes using optical microscopy, and their rigidity makes them incompatible with mechanical sectioning for transmission electron microscopy (TEM) characterization.[20] Furthermore, the high precision offered by inorganic NNs comes at the expense of increased fabrication complexity, cost of manufacturing, and throughput.[21] NN

transfer or replication methods are therefore urgently needed to increase fabrication efficiency and flexibility, while simultaneously accommodating requirements for optical transparency and tunable physico-chemical properties.

Recent developments in nanofabrication techniques offer the potential to transfer or replicate vertically and horizontally configured nanostructures from one substrate to another, through (i) nanotransplantation printing;[22] (ii) transfer techniques into recipient substrates such as PDMS or glass;[23] and (iii) replication routes (casting, imprinting, molding).[24] But substrate transfer processes can be labor-intensive, offer only limited reproducibility, and come with the risk of compromising the integrity of the original nanostructures. By contrast, nanostructure replication approaches are rapid, cost-effective, highly reproducible, and versatile, allowing production of multiple copies of the same nanostructured array from a wide range of materials with just one master mold. Polymers are an particularly useful class of materials for such replication approaches, combining cost-effectiveness with high optical transparency, biocompatibility, and flexibility in chemical modifications. These features have made polymeric NNs a functional and versatile platform for a variety of cellular manipulations and interrogations.[25] So far, polymeric NNs have been used in intracellular signaling studies,[26] anti-bacterial and anti-biofouling applications,[27] biomedical sensing and cellular probing,[28] and neuron and stem cell research.[29]

In this study we fabricated polymeric NNs using PS, SU8, and PDMS to achieve dynamic cellular contact with both adherent cells (GPE86 mouse embryonic fibroblasts) and non-adherent cells (L1.2 mouse immune B cells). Our cytocompatible polymeric NNs were used to probe cell behavior, including cell morphology, focal adhesion complex development, viability, apoptosis, proliferation, and migration. Importantly, our PS, SU8, and PDMS NNs all delivered mRNAs into both GPE86 and L1.2 cells. Transfection efficiencies of

49.4%±11% and 12±7% was achieved for GPE86 cells and L1.2 cells, respectively. We showed that enhanced endocytosis involving caveolin-1 (CAV-1) and clathrin heavy chain (CHC) is a mechanism of PS NN-mediated intracellular delivery.

2. Results and discussions

2.1. Design and fabrication of polymeric NNs

In our earlier work we developed conical Si NN arrays as a platform to induce cellular deformation and facilitate gene delivery for both adherent and nonadherent cells.[30] But this Si NN platform suffers from several drawbacks: a lack of optical transparency; complex and costly fabrication process and equipment; and limited scalability. By replicating Si NNs into polymeric NNs we can harness the advantages of polymeric materials while retaining the precise nanotopography of the Si NN master template.

2.1.1. Negative mold fabrication

We first designed and fabricated tunable Si NN arrays with a conical profile (height 3.5 μm; pitch 3 μm; tip diameter 100 nm) (**Figure 1**a i), which acted as a master template for producing PDMS negative molds (Figure 1a ii,iii). Each master Si template was silanized with an anti-adhesive, trichloro(1H,1H,2H,2H-perfluoro-octyl)silane, to minimize the adhesion of the casted PDMS (Figure 1a ii). Upon curing and template removal, a negatively replicated mold of the master Si NN arrays (an array of holes) was generated (Figure S1). The mold was then silanized prior to polymeric NN fabrication to facilitate detachment of the replicated polymeric NNs from the mold.

2.1.2. Replication of polymeric NNs

We chose nanoimprint lithography (NIL) over other polymer fabrication techniques for producing PS and SU8 NNs because of its cost-effectiveness, and its ability to pattern a variety of polymeric materials and to precisely control geometrical features over a large scale.[31] A PDMS casting method was used to fabricate PDMS NNs. Thermoplastic PS NNs were fabricated using thermal NIL, by pressing the pre-fabricated PDMS negative mold onto the prepared flat PS substrate (Figure 1b i) under constant pressure (Figure 1b ii). A Si wafer backing maintained the flatness of the PS substrate and ensured efficient heat transfer. During the molding stage we heated the PS substrate above its glass transition temperature (Figure 1b iii). Constant pressure was maintained until PS NNs were cooled to set. The mold was removed to obtain the replicated PS NNs (Figure 1b iv). Similarly, SU8 NNs were fabricated using UV-NIL where SU8 was first coated on the glass substrate (Figure 1c i), and then pressed by the pre-fabricated PDMS negative mold (Figure 1c ii). During UV-NIL we maintained the negative mold at constant pressure by the NIL air cushion to press over the SU8-coated glass substrate during UV curing (Figure 1c iii). SU8 NNs were obtained upon mold removal (Figure 1c iv). The same mold was used to fabricate PDMS NNs. PDMS was coated onto the glass substrate (Figure 1d i) and pressed by the silanized, pre-fabricated PDMS negative mold (Figure 1d ii). The PDMS NNs were placed in vacuum to degas and left for polymerization (Figure 1d iii). PDMS NNs were obtained upon mold removal (Figure 1d iv). Taken together, these processes enabled the fabrication of three types of polymeric NNs—PS, SU8, and PDMS—that exhibit the same average geometry: height 3.5 μm, tip diameter 250 nm, and pitch 3 μm, as confirmed by scanning electron microscopy (SEM) (**Figure 2**a–c) and laser scanning confocal microscopy imaging (Figure 2d).

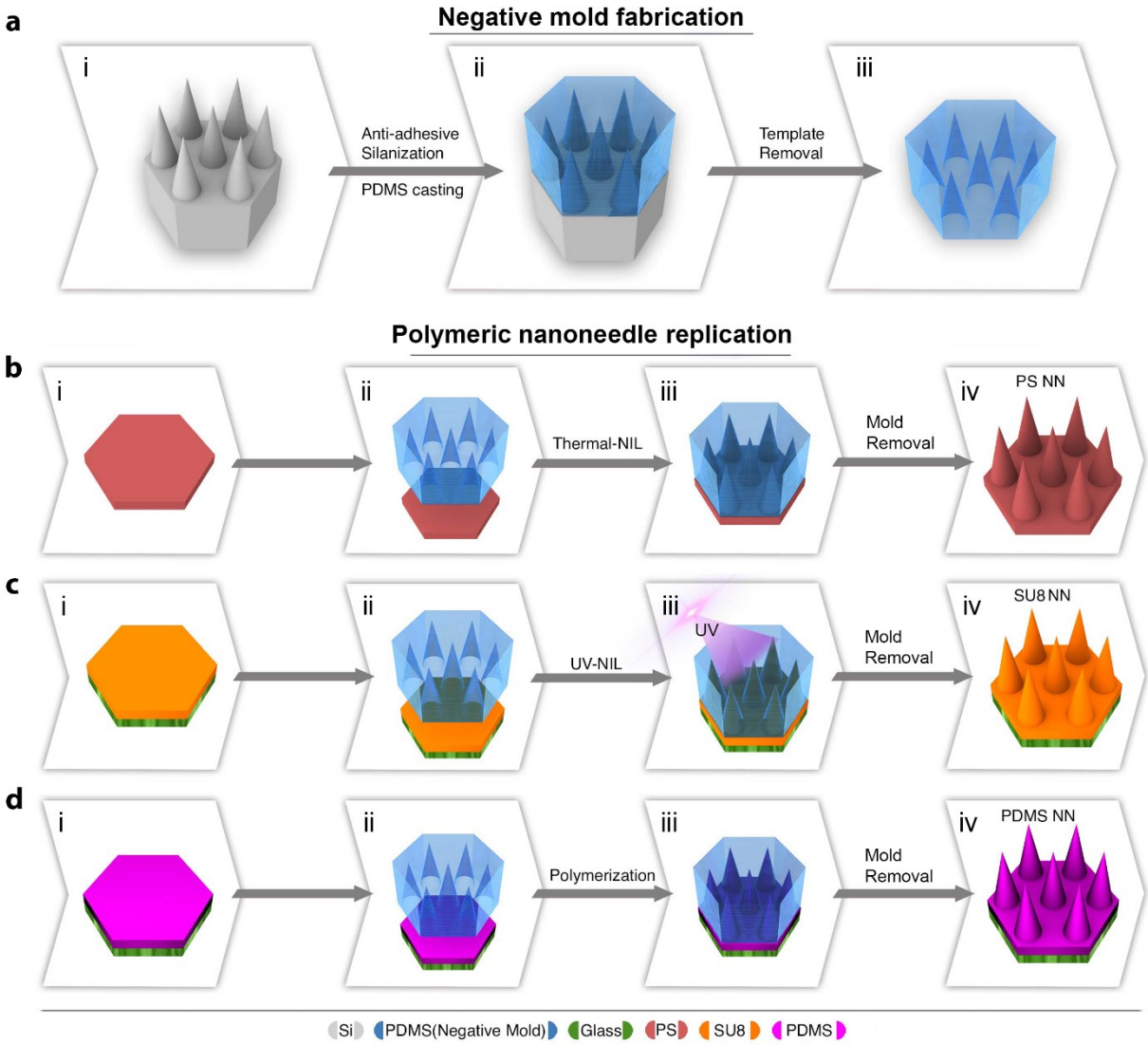

Figure 1. Polymeric NN fabrication workflows. *(a) Negative mold fabrication.* (i) The Si NNs master mold was first silanized and (ii) casted with PDMS, which was left to cure. (iii) The Si NNs template was removed after curing to obtain the negative PDMS mold. The negative PDMS mold was silanized prior to polymeric NN replication. *(b–d) Polymeric NN replication.* (b) PS NN fabrication. (i) The PS substrate was prepared and (ii) pressed by the PDMS mold during (iii) thermal NIL, where the PS was heated above its glass transition temperature while in contact with the negative mold. (iv) PS NNs were obtained upon negative mold removal. (c) SU8 NN fabrication. (i) SU8 was coated on a glass slide. (ii) The prepared PDMS mold was pressed onto the SU8-coated glass slide. (iii) This was followed by UV-NIL. (iv) SU8 NNs were obtained upon mold removal. (d) PDMS NN fabrication. (i)

PDMS was coated on a glass slide. (ii) The prepared PDMS mold was pressed onto the PDMS-coated glass slide and left in a vacuum to degas for 1 h, followed by (iii) curing (polymerization) in an oven at 65 °C for 2 h. (iv) PDMS NNs were obtained upon mold removal.

Figure 2. Three types of polymeric NNs. SEM images of (a) PS, (b) SU8 and (c) PDMS NN arrays replicated from a Si NNs master mold with magnification of (i) 1500X (ii) 5000X and (iii) 30000X. d) Top (i) and (ii, iii) 3D view of laser scanning confocal microscopy images of SU8 NNs.

2.1.3. Stiffness of polymeric NNs

Different polymeric NNs have different chemical compositions and stiffness, which can affect the cell–NN interface. For example, the surface energy and wettability of a polymer can influence cell attachment and spreading,[32] and polymer mechanical stiffness can influence the activation of mechanotransductory signaling pathways and affect cell phenotype,[24b,33] stem-cell differentiation,[34] adhesion and traction-force generation,[35] migration and proliferation,[36] and gene expression.[36a,37]

We used *in situ* SEM nanoindentation to calculate the Young's modulus value[38] to measure the stiffness of our polymeric NNs and compare it with that of the Si master. NNs were bent by an *in situ* nanoindentation tip using various indentation forces of 500–5000 μN (Figure S2a, Movie S1). We identified three stiffness regions: high-stiffness Si NNs (~140 GPa, consistent with reported values[39]), medium-stiffness PS and SU8 NNs (~1.5 and ~2.5 GPa respectively), and low-stiffness PDMS NNs (~0.014 GPa) (Figure S2b). Fabricating the same geometry NNs with varied stiffness allows us to decouple the two parameters and examine solely the effect NN stiffness has on cell behavior (discussed further below). Furthermore, by using different types of polymeric materials with the same surface

modification, a wider stiffness range with exact topography and functional surface can be fabricated. For example, the PDMS stiffness can be controlled between 800 kPa to 10 MPa, the inclusion of PS can expand the range of stiffnesses into GPa region.[40] The Young's modulus of cells is in the range of 0.1 – 100 kPa,[41] hence interfacing cells with medium to low stiffness polymeric NNs, as compared to high stiffness Si NNs, can minimize the mismatch of cell–NN stiffness and increase the interface compatibility.

2.2. Cell–polymeric NN interfaces

Cell morphology, cytoskeletal arrangement and formation of focal adhesion complexes are essential to maintaining an intimate and functional cell–NN interface—crucial especially for cell manipulation via mechanotransduction,[2a,10a,29b] intracellular probing,[6e,26a,42] and cargo delivery.[2b,30,43] Different types of cells can perceive and respond differently to mechano-instructive cues, including topographical and mechanical stimuli.[1a,1b] A central challenge at engineered cell–NN interfaces is to understand how to decouple substrate topography and stiffness, since each on its own or in combination can influence cell behavior and function.[44] To decipher what impact, if any, substrate stiffness has on cell topography-induced responses to NN interfacing, we probed the morphology and focal adhesion complex formation of both adherent and non-adherent cells interfaced with arrays of PS, SU8, and PDMS NNs.

2.2.1. Cell morphology on polymeric NNs

We first functionalized polymeric NNs using poly-D-lysine (PDL)—a positively charged molecule that improves cell attachment by interacting with the negatively charged lipid bilayer of the plasma membrane.[45] We then seeded GPE86 and L1.2 cells on PS, SU8, and PDMS NNs, and applied centrifugal force (250 g, 32 °C, 15 minutes) to assist the interfacing. After 6 h incubation, cell–NN samples were processed for SEM imaging to observe the morphology of cells attached to the NNs—an initial indicator of cytocompatibility. Selected

tilted SEM images showed that GPE86 cells on PS (**Figure 3**a i) had two morphologies: flattened and elongated, and round with less spreading. Closer observation of the interface revealed that flattened, elongated GPE86 cells spread over multiple PS NNs with extended lamellipodia, out of which protruded filopodia (Figure 3a ii); but that rounder GPE86 cells interacted with fewer NNs. PS NNs were deflected by the GPE86 cells, which were absent on the stiff Si NNs.[30] GPE86 cells on SU8 NNs showed mainly flattened and elongated morphology with long filopodia protrusions (Figure 3b i). This effective cell spreading resulted in visible NN indenting the bottom of the cells (Figure 3b ii). We observed similar deflections of SU8 NNs to those we saw for the PS NNs. By contrast, GPE86 cells on PDMS NNs showed mainly round morphology with minimal spreading (Figure 3c i). Filopodial protrusions from the cells interacted with multiple PDMS NNs, pulling them toward the cell body (Figure 3c ii). Aside from NN deflection, most of the PDMS NNs—which have the lowest stiffness of all NNs—collapsed after forceful interfacing with GPE86 cells. To determine what contributed to this collapse, we centrifuged PDMS NNs without seeding cells on them and processed the samples in the same way we prepared samples for cell–NN interface imaging. PDMS NNs showed no significant difference before (Figure S3a) and after (Figure S3b) the processing. We further investigated if the height of PDMS NN contributed to collapse, by interfacing shorter PDMS NNs (3 μm height, similar to NN pitch) with GPE86 cells, observing no collapse after forceful interfacing (Figure S4a,b). These results showed that GPE86 cells collapse the PDMS NNs, especially when NN height is larger than NN pitch.

Unlike GPE86 cells, L1.2 cells mostly retained their globular shape on all polymeric NNs, and interacted with fewer NNs per cell (Figure 3d–f). Unsurprisingly, deflection of NNs occurred across all samples for L1.2. There was also deflection of PS, SU8, and PDMS NNs interacting with the edges of L1.2 cells (Figure 3d ii, 3e ii, 3f ii). Collapse of PDMS NNs was

much less when interfaced with L1.2 cells than with GPE86 cells. Very few cells were attached on PDMS NNs compared with PS and SU8 NNs. This agrees with cell counts measured by live/dead cell staining, where L1.2 cell counts attached to PDMS NNs (87 cells mm^{-2}) were significantly lower than for PS (2643 cells mm^{-2}) and SU8 NNs (1465 cells mm^{-2}) (Figure S5). Difference in cell counts between cells attached to PS and SU8 NNs did not reach significance. Studies showed that substrate stiffness can impact cellular behaviors in different cell types, where it can influence the cell's adhesion and traction-force generation,[35] migration and proliferation,[36] our result suggests that L1.2 cells do not attach well on soft PDMS NNs (~0.014 GPa) compared with the stiffer PS and SU8 NNs (~1.5 and ~2.5 GPa, respectively). Due to profoundly low number of L1.2 cells attached on PDMS NNs, we conducted all following PDMS NNs experiments with only GPE86 cells but not L1.2 cells.

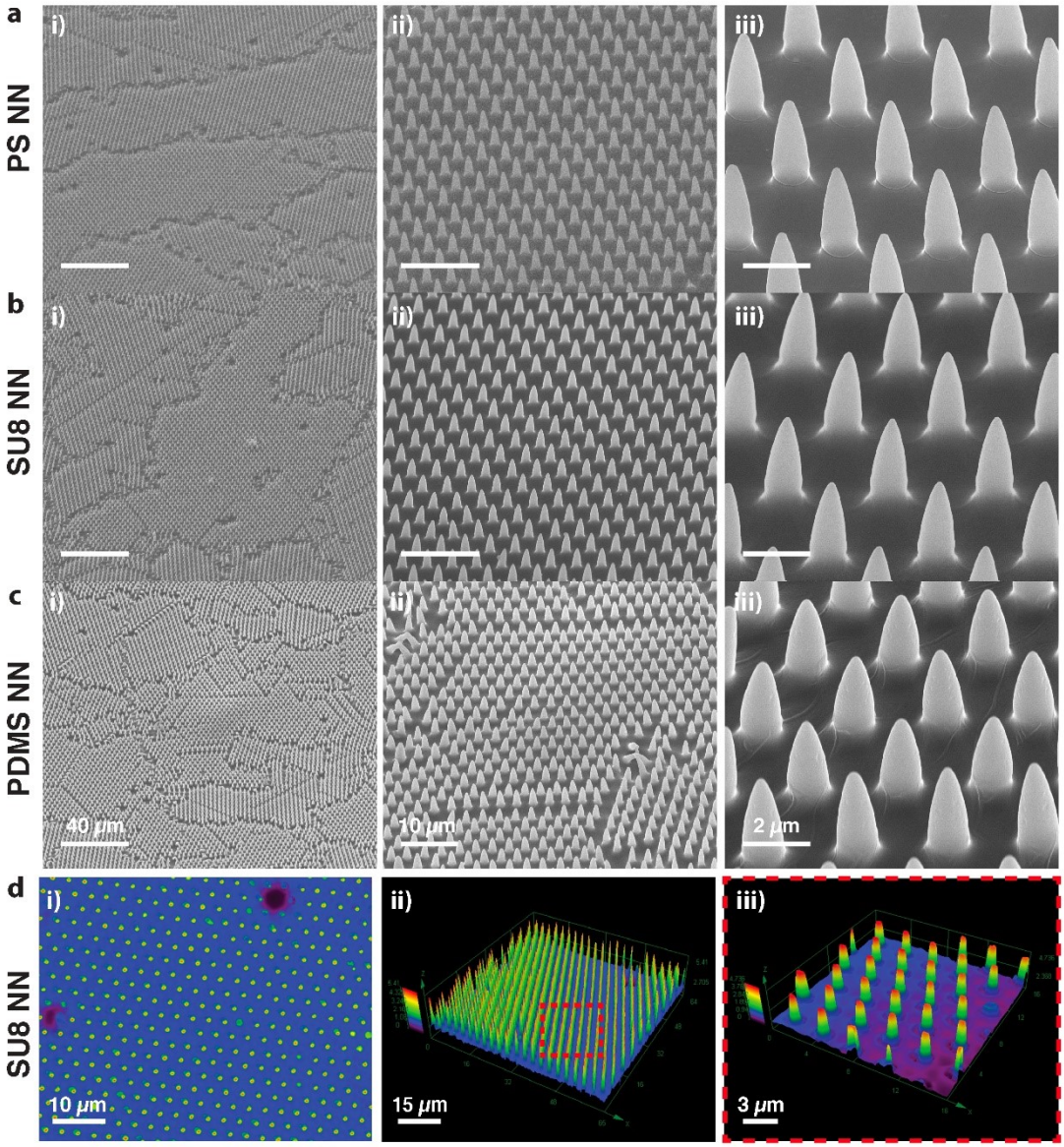

2.2.2. Formation of focal adhesion complexes on polymeric NNs

The formation and maturation of focal adhesion complexes are critical for cell migration and regulation of mechanical and biochemical signaling pathways.[46] To understand cell adhesion status at the cell–NN interface, we employed immunofluorescence to determine the distribution of three focal adhesion complex-associated proteins: F-actin (a cytoskeletal filamentous actin), vinculin (a membrane-cytoskeletal protein and a key component of focal adhesion complexes), and β-integrin (a transmembrane receptor)—all of which can influence focal adhesion formation and thus cell attachment to polymeric NNs.

Figure 3g displays GPE86 cells grown on PS NNs; dark spots—appearing periodically, in the same pattern as the NNs—were observed in the nuclei stained with Hoechst 33342 (Hoechst, blue), suggesting a possible nuclear deformation by the PS NNs.

GPE86 cells on PS NNs formed ring-shaped F-actin (red) around the NNs (Figure 3g, Figure S6a, Movie S2); this suggests that PS NNs stimulated actin polymerization, possibly due to membrane curvature induced by the NNs.[16b] Vinculin (green) and β-integrin (purple) interacted with the PS NNs at the cell peripheries, showing colocalization at the edges of filopodial protrusions. As β-integrin is known to recruit vinculin toward the cell membrane to form focal adhesions,[47] their colocalization indicates formation of focal adhesion complexes around PS NNs; consistent with what has been reported with polymeric NNs of similar Young's modulus (1.2 GPa).[48] GPE86 cells on SU8 NNs had similar F-actin rings around the NNs (Figure S7a) to those seen on PS NNs, which were absent on the flat SU8 control (Figure S7b). Vinculin and β-integrin were observed at the cell periphery on SU8 NNs, similar to PS NNs. GPE86 cells formed ring-shaped F-actin around PDMS NNs, which were less ordered than for SU8 and PS NNs (Figure S7c); most likely since PDMS NNs were easily deflected by GPE86 cells as mentioned earlier. The distribution of vinculin and β-integrin on GPE86 cells—interfaced with PDMS NNs—were similar to those observed for PS and SU8 NNs. There was no difference in F-actin, vinculin, or β-integrin distribution on flat PDMS and PDMS NNs (Figure S7d). Taken together, these results suggest that formation of focal adhesion complexes by GPE86 interfaced with polymeric NNs is likely to be stiffness-independent.

For L1.2 cells on PS NNs, we found that F-actin aggregates along the short filopodial protrusions and along the cell membrane, while vinculin and β-integrin were distributed throughout the cytoplasm (Figure 3h, Figure S6b, Movie S3). L1.2 cells on SU8 substrates also showed no accumulation of F-actin, vinculin, or β-integrin on either NNs or the flat control (Figure S7e,f). So neither PS nor SU8 NNs induced focal adhesion formation in L1.2 cells.

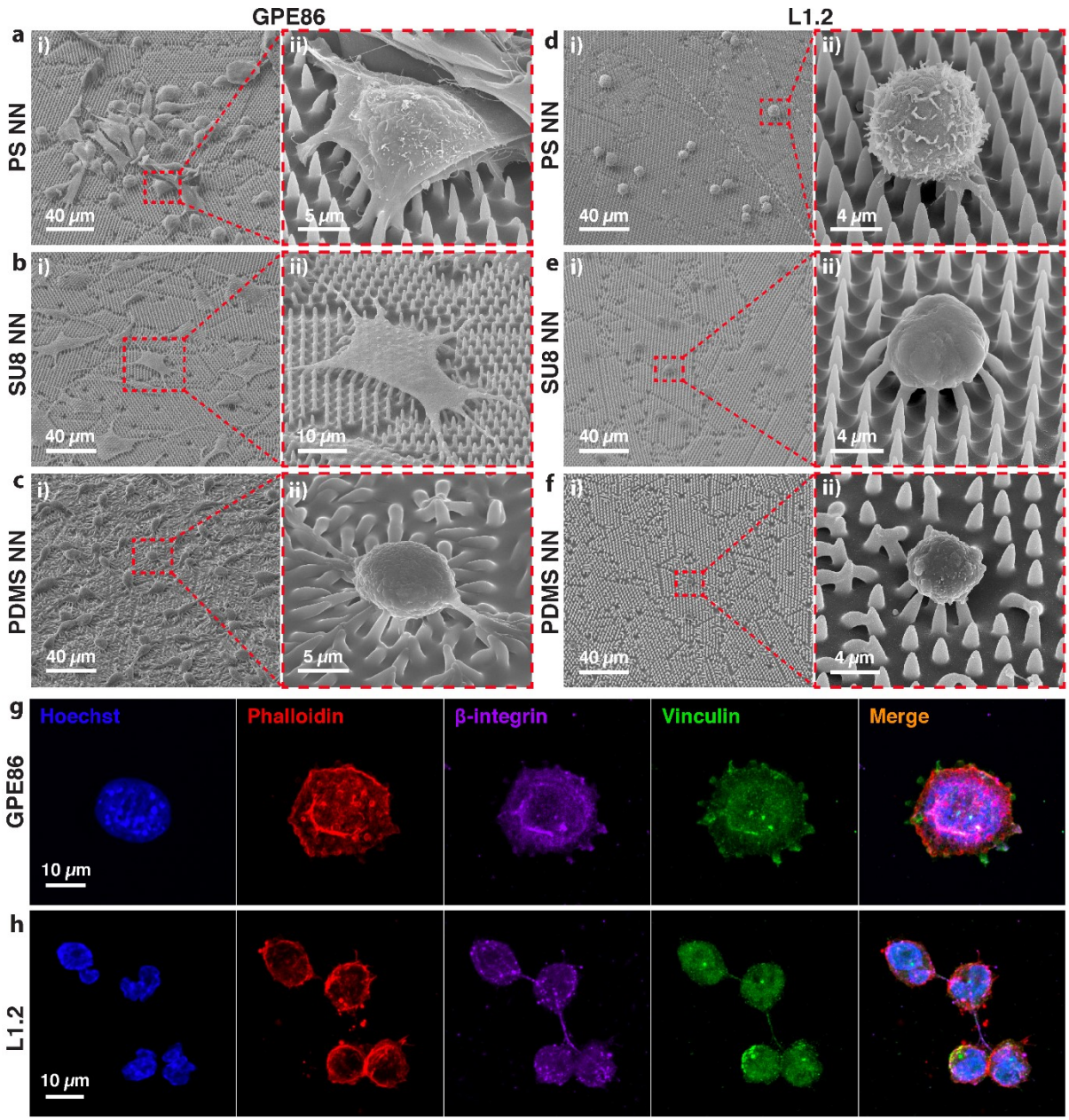

Figure 3. The cell–polymeric NN interface. Tilted SEM images (45°) of (a–c) GPE86 and (d–f) L1.2 cells interfaced on (a,d) PS, (b,e) SU8, and (c,f) PDMS NNs, with (i) overview and (ii) enlarged views of the regions marked by red squares. Maximum-intensity projection of z stacks using confocal microscopy of (g) GPE86 and (h) L1.2 cells on PS NNs. Cells were fixed and stained with phalloidin (red), Hoechst 33342 (blue), anti-vinculin (green), and anti-β-integrin (purple) to reveal F-actin, nucleus, and distribution of vinculin and β-integrin, respectively.

2.3. Cell health and growth on polymeric NNs

To demonstrate the cytocompatibility of the PS, SU8, and PDMS NNs, we investigated cell health and basic cell functions by performing viability, apoptosis, proliferation, and migration assays; this can help to determine whether interfacing with PS, SU8, and PDMS NNs induce undesirable cell perturbation and/or damage, and more importantly whether cells maintain their proliferative capacity after detachment from the NNs, important for later evaluating intracellular delivery efficacy.

2.3.1. Viability and apoptosis

Given that cell viability is required for a functional and biocompatible cell–NN interface,[32a] we assessed the viability of GPE86 and L1.2 cells on both polymeric NNs, using fluorescein diacetate (FDA)/propidium iodide (PI) (live/dead) staining, with flat substrates as a control. Confocal microscopy revealed the live (green) and dead (red) GPE86 and L1.2 cells on a representative PS substrate (Figure S8a,b). Both GPE86 and L1.2 cells displayed a high viability of 99% on both PS and SU8 NNs, similar to that on flat control (Figure S8c,d). GPE86 cells had significantly lower viability of 96% on PDMS NNs than PS and SU8 NNs, and 97% on the flat PDMS control (Figure S8c).

Apoptosis evaluates the onset of programmed cell death.[43,49] To determine whether interfacing with polymeric NN induces apoptosis, we used the Caspase-Glo 3/7[50] luminescence assay to probe apoptosis after 2, 6, and 24 h interfacing with each of PS, SU8, and PDMS NNs. Untreated and propranolol-treated cells served as negative and positive controls, respectively.[51] Using a plate-reading luminometer we measured the luminescence of each sample, proportionate to caspase-3/7 activity (caspase 3 and 7 are both activated in apoptosis,[52] hence caspase-3/7 activity is an indicator of cell apoptosis). Between 2 h and 24 h, GPE86 cells on PS, SU8, and PDMS NNs, and their corresponding flat substrates, showed similar luminescence intensity to that of untreated cells, indicating no increase in caspase-3/7

activity or apoptosis (**Figure 4**a, left). This finding is in accordance with previous reports that GPE86 cells on Si NNs of similar geometry do not produce increased caspase-3/7 activity or apoptosis in these cells during this time frame.[30]

For L1.2 cells, the luminescence intensity of PS and SU8 NN samples was not significantly different from those of flat and negative control samples at 2 h and 6 h (Figure 4a, right); this indicated no apoptosis-associated caspase-3/7 activity up to 6 h. However, at 24 h we detected a significantly stronger luminescence signal in L1.2 cells on SU8 NNs, indicating enhanced caspase-3/7 activity; this suggests that prolonged (up to 24 h) culture of L1.2 cells on SU8 NNs can ultimately lead to apoptosis. This elevated caspase activity at 24 h was not observed for L1.2 cells on PS NNs. So for the following studies we chose 6 h as the NN interfacing time, which has proven to be sufficient for intracellular delivery[2b] while minimizing any negative impacts on cell viability.

2.3.2. Proliferation

Cell proliferation is another key factor for evaluating the impact of NNs on cell health and growth.[25c] NNs can affect cell proliferation by influencing the reorganization of the nucleus and cytoskeleton during mitosis,[2a,10a] so it is important to assess cell proliferation post NN-interfacing. The maintenance of cell proliferation capability is also essential for NN-mediated intracellular delivery, since it can influence delivery efficacy especially for nucleic acids,[53] and NN-transfected cells need to be viable and proliferative for subsequent *in vitro* or *in vivo* functional studies.[9] We performed a proliferation assay to detect the impact of NNs on the frequency of cell mitosis. GPE86 and L1.2 cells were first labeled with a division-tracking dye, CellTrace Violet (CTV), before seeding onto PS, SU8, and PDMS NNs. After 6 h incubation, cells were detached from NNs by either trypsinization (GPE86 cells) or gentle pipetting (L1.2 cells). One set of harvested cells were immediately analyzed by flow

cytometry (6 h), and the rest were cultured in fresh media and analyzed after 24 h and 48 h. CTV covalently binds to intracellular proteins in the cytoplasm and nucleus, and halves in fluorescence intensity with each round of cell division; so, the continuous reduction of CTV signal in both GPE86 and L1.2 cells from 6 h to 24 h to 48 h indicates that cells from both types have undergone proliferation after NN detachment (Figure 4b). For both GPE86 and L1.2 cells there was no significant difference in the normalized CTV signal between each polymeric substrate (Figure 4b). To further examine the division numbers of each cell type, we used ModFit LT (a flow cytometry histogram modeling software) to analyze the CTV-dilution pattern of GPE86 and L1.2 cells over eight generations. By 48 h, a major peak at generation 3 (magenta) showed that most GPE86 cells had undergone ≥ three divisions, and a major peak at generation 5 (yellow) showed that most L1.2 cells had undergone ≥ five divisions (Figure 4c). Both cell types maintain proliferation capacity post NN-interfacing, especially for GPE86 cells, for which we observed stiffness-independent proliferation profile for PS, SU8 and soft PDMS NNs (~1.5, ~2.5 and ~0.014 GPa, respectively).

2.3.3. Cell migration

To investigate cell migration on polymeric NNs in real-time, we performed live-cell imaging using confocal microscopy. The optical properties of polymeric NNs offer an alternate imaging platform to opaque vertically aligned NNs such as Si NNs, requiring no fluorescence staining of the NNs for visualization by means of an inverted live-cell imaging microscope.[28b,54]

We seeded GPE86 cells (expressing mCherry fluorescence protein) onto PS, SU8, and PDMS NNs, and followed their migration over 12 h. Live-cell imaging showed that GPE86 cells spread with extended membrane protrusions, interacted with their surrounding cells, and migrated over the PS NNs (Movie S4, Hoechst/mCherry/transmission channel).

Lamellipodium extension was generated by GPE86 cells on PS NNs, driven by the combination of actin polymerization and adhesive complex formation.[55] The trajectory was recorded over 12 h and the total migration length statistically analyzed for individual GPE86 cells; the median GPE86 migration length was ~111, ~92, and ~115 μm on PS, SU8, and PDMS NNs, respectively (Figure S9a). Substrate stiffness can have a negative impact on fibroblast cell migration,[56] but we observed no significant differences in migration length between stiffer PS and SU8 NNs compared to softer PDMS NNs. The median migration length for flat substrates were ~153, ~115, and ~95 μm on PS, SU8, and PDMS NNs, respectively (Figure S9a); flat PS showed significantly increased median GPE86 cell migration length compared to PS NNs, but median migration length was significantly less on flat PDMS than for PDMS NNs. There was no significant difference in median migration length between the three polymeric NNs.

Unlike GPE86 cells, L1.2 cells on PS NNs showed little to no morphological change during migration (Movie S5, Hoechst/transmission channel). The median migration length for L1.2 cells on PS NNs (~151 μm) was significantly higher than those on SU8 NNs (~100 μm) (Figure S9b). We observed no significant difference in migration length between PS NNs and flat PS; but the L1.2 cells on flat SU8 had a significantly increased migration length of ~125 μm compared to the SU8 NNs.

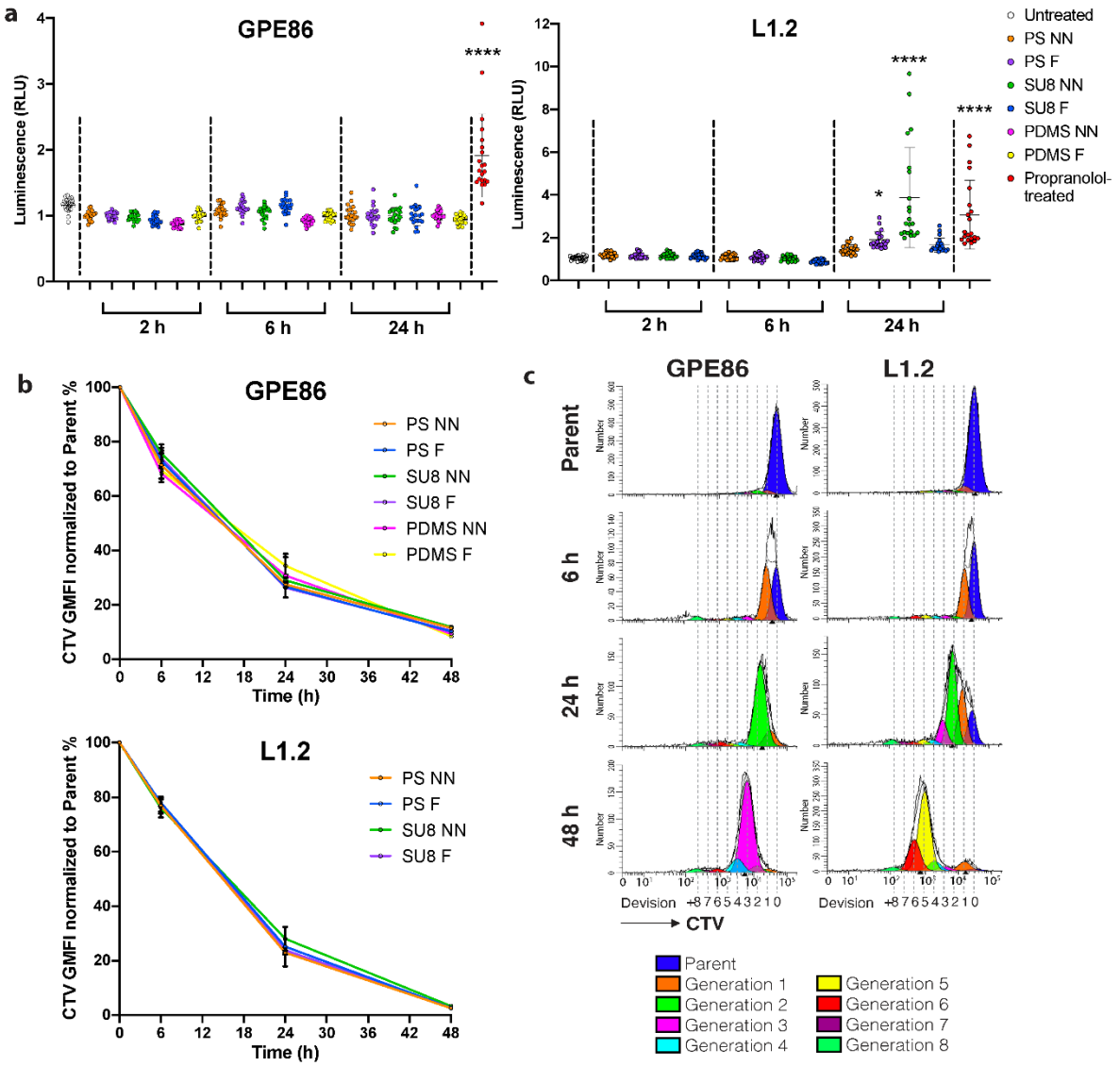

Figure 4. Cell apoptosis and proliferation. (a) Luminescence intensity of (left) GPE86 and (right) L1.2 cells on PS, SU8, and PDMS NNs and their corresponding flat ("F") substrate controls over 2, 6, and 24 h, with untreated and propranolol-treated cells as negative and positive controls, respectively. RLU, relative light unit. ****P < 0.0001 (one-way ANOVA), n=3. (b) Flow cytometry analysis showing quantification of CTV GMFI within detached GPE86 cells (interfaced with PS, SU8, and PDMS NNs, and their corresponding flat substrate) and L1.2 cells (interfaced with PS and SU8, and their corresponding flat substrates) at 6, 24, and 48 h. Cells before NN interfacing (0 h) were the parent control, and unstained

cells were the negative control. n = 3. (c) ModFit LT analysis of the CTV-dilution pattern of GPE86 and L1.2 cells over eight generations at 6, 24, and 48 h after interfacing with PS NNs.

2.4. Polymeric NNs for intracellular delivery

NNs, especially Si NNs, can facilitate intracellular delivery (nanoinjection) of diverse cargos such as nucleic acids,[2b,10d] gene-editing tools,[4,10d] proteins,[4,57] and nanoparticles,[43,58] into mammalian cells and tissues. Nanoinjection has enabled advanced *in vitro* and *in vivo* cellular manipulation with negligible impact on cell viability and function.[9,10d,23b] But vertically aligned polymeric NNs have rarely been used for nanoinjection. As a nonintegrating 'footprint-free' route for inducing protein expression, mRNA delivery has become increasingly important for regulating transcription factor expression and signaling cascades, with reduced risk of mutagenesis compared to pDNA and off-target effects owing to the natural decay of mRNA during the cell cycle.[10d,59]

We delivered Cy5-tagged mRNAs encoding a GFP reporter (Cy5-GFP-mRNA) into GPE86 and L1.2 cells. The loading of mRNAs on NNs was first verified. PS NNs were functionalized with positively charged PDL, required for loading the negatively charged Cy5-GFP-mRNAs. Without PDL, mRNAs were unable to be loaded onto the NNs (Figure S10a). Confocal imaging confirmed that mRNAs were evenly loaded on individual PS NNs across the entire substrate (Figure S10b–d). We then seeded GPE86 and L1.2 cells onto mRNA-loaded polymeric NNs, followed by centrifugation. The cultured GPE86 cells were harvested by trypsinization whereas L1.2 cells were dislodged from the NNs by gentle pipetting after 6 h incubation.

Flow cytometry was used to determine the transfection efficiency of both cells. Transfection efficiencies were indicated by gating the population that was both Cy5 and GFP positive (**Figure 5**a). Cy5 positivity indicated successful intracellular delivery, and GFP positivity indicated successful transfection. For GPE86 cells, 26.8±3.5%, 33.2±7.4%, and 30.1±4.1% average transfection efficiencies were achieved by PS, SU8, and PDMS NNs, respectively (Figure 5b). There was no significant difference between each polymeric NN; the efficiencies were significantly higher than those of their flat counterparts (4.4±1.9%, 7.4±1.3%, and 6.5±2.5%, respectively). For L1.2 cells, 9.5±1.8% and 12.5±6.5% transfection efficiencies were recorded for cells harvested from PS and SU8 NNs (Figure S11a, b); PS and SU8 flat controls both showed ~1% transfection efficiency. These data strongly suggest that transfection can be achieved using polymeric NNs, despite their much lower stiffness than their Si counterpart.[30] For GPE86 cells in particular, transfection mediated by polymeric NNs is not stiffness-dependent, given that similar efficiencies were achieved by the low-stiffness PDMS NNs, and the stiffer PS and SU8 NNs. The lower transfection efficiency seen for L1.2 cells might result from the reduced cell-NN interaction due to their rounded morphology compared to GPE86 cells, and the sophisticated regulatory network of immune cells, involving cytoskeletal reorganization,[60] activation of immune pathways,[61] and enhanced immune responses[26b,26c] activated upon mechanical stimulation.

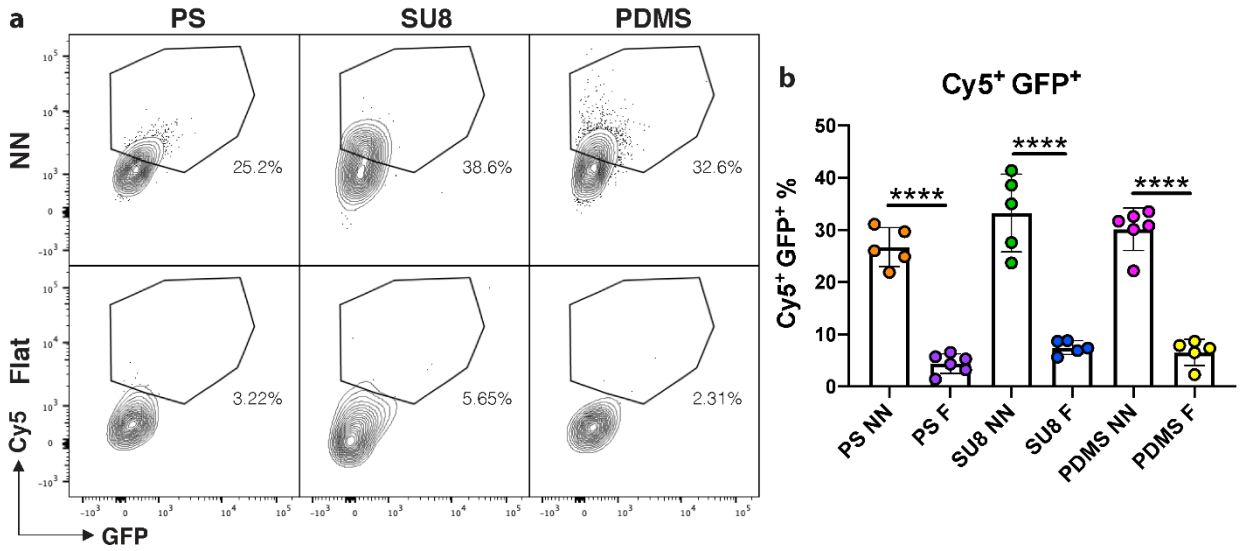

Figure 5. NN-mediated intracellular delivery of Cy5-GFP-mRNA into GPE86 cells. (a) Flow cytometry analysis of $Cy5^+$ GFP^+ population with GPE86 cells detached from mRNA-coated PS, SU8, and PDMS NN, along with their flat counterpart ("F"), after 6 h incubation. Non-transfected cells served as the negative control. (b) Quantification of $Cy5^+$ GFP^+ population within transfected GPE86 cells. ****$P < 0.0001$ (one-way ANOVA), $n \geq 5$.

2.5. Cellular deformation and endocytosis induced by polymeric NNs

To better understand how polymeric NNs facilitate the delivery of mRNA, it is important to probe the underlying mechanisms that govern intracellular delivery. Three proposed delivery mechanisms are involved in nanoinjection: spontaneous penetration by NNs,[43,62] membrane permeabilization,[5d,63] and NN-induced endocytosis.[2b,30] The mechanism by which nanoinjection occurs is still subject to intense debate.[1a,1b,17] Since vertically aligned polymeric NNs had rarely been used for nanoinjection, the mechanism at play here needed to be investigated. High-resolution electron microscopy techniques such as FIB-SEM and TEM can reveal, to some extent, cell responses to membrane-associated physical stimuli, enabling insights into underlying NN-mediated cargo delivery mechanisms.[2b,20,42] This is essential for designing more effective nanoinjection platforms. We employed FIB-SEM and TEM

combined with immunofluorescence, to characterize the interface between GPE86 and L1.2 cells and polymeric NNs, and to identify parameters that might contribute to the different transfection efficiencies between the two cell types.

2.5.1. FIB-SEM characterization

We first used FIB-SEM for cross-sectional imaging of the cell–polymeric NN interface via iterative FIB milling. GPE86 cells showed plasma membrane deformation (**Figure 6**a i) and ruffling (Figure 6a ii) around the PS NNs, which did not pierce the plasma membrane but remained engulfed within the cell body. Deformed cellular membranes may temporarily lose integrity to allow bioactive cargo to enter the cell. [5d] In addition, the curvature of the deformed membrane on NNs is known to trigger localized endocytic protein accumulation via curvature-sensitive proteins. [2b,42] Similar plasma membrane deformation and ruffling were also observed on SU8 (Figure S12a i,ii) and PDMS NNs (Figure S13a i) where some of the NNs were deflected during the interfacing, while others interacted with the cell by slightly deforming the nucleus (Figure S13a i) and the plasma membrane (Figure S13a ii).

For L1.2 cells interacting with PS NNs, the plasma membrane deformed around the NNs (Figure 6b i) but just like for GPE86 was not pierced by the NNs (Figure 6b ii). Remodeling of the nuclear membrane was also observed in L1.2 cells interfaced with PS NNs (Figure S14a,b). SU8 NNs gave rise to similar plasma membrane deformation and nuclear membrane remodeling (Figure S12b i,ii). Just like for GPE86 cells, membrane penetration was not evident.

To further enhance high-resolution characterization of nanoinjection delivery mechanism and cell–NN interfacial interaction, we use TEM and immunofluorescence as complementary methods to the FIB-SEM analysis.

2.5.2. TEM characterization

TEM is a highly effective approach for imaging cell–material interfaces at the nanoscale.[6e,64] It can reveal high-resolution structural information about cells that is inaccessible by FIB-SEM. We generated lamellae of the cell–NN interface with minimal artefacts for efficient TEM identification and characterization of interfacial interactions. The new method allowed us to simultaneously screen NN interactions within single and multiple cells with greater resolution and contrast, and to investigate if endocytic vesicles (e.g., caveolae and clathrin-coated vesicles) were induced at the periphery of the NNs, as reported earlier for Si NNs.[2b,42] Only PS and PDMS NNs were selected for TEM characterization because SU8 NNs were attached to a hard glass substrate, limiting the direct sectioning option (PS NNs were not attached to any substrate, and PDMS NNs can be detached from the glass substrate for direct sectioning).

Nanometer-resolution TEM imaging of the lamellae revealed the tight interfacial interaction between both GPE86 and L1.2 cells with PS NN arrays, and GPE86 cells with PDMS NN arrays. The black dot arrays are the PS NN elements that have been sectioned by ultramicrotome (Figure 6c i). Closer examination revealed the presence of endocytic pits and vesicles (indicated by yellow arrows) at the GPE86 cell–PS NN interface (Figure 6c ii,iii) suspected to be caveolae or clathrin-coated pits due to their size (<100 nm in diameter).[65] For PDMS NNs, we found similar black dot arrays indicating the NN elements (Figure S13b i) and multiple endocytic pits indicated by yellow arrows, formed at the periphery of NNs (Figure S13b ii-iii). Interestingly, TEM imaging of L1.2 cells demonstrated in contrast a smooth interaction with the PS NNs, without the presence of vesicles around the PS NNs (Figure 6d i–iii).

On the basis of both FIB-SEM and TEM imaging, the distinctive membrane invaginations of the endocytic pits were manifested at the periphery of PS and PDMS NNs in the case of GPE86 cells. This suggests the activation of endocytic pathways induced by NNs,[2b,30,42] which in turn might have contributed to the higher mRNA transfection efficiency achieved in GPE86 cells compared with that seen for L1.2 cells.

2.5.3. Immunofluorescence characterization by means of confocal microscopy

We characterized the cell–NN interface using immunofluorescence staining and confocal microscopy,[16b,26a] to investigate the role of the distribution of endocytic components in NN-mediated delivery. In particular, two endocytosis-associated proteins were investigated: CAV-1, a scaffolding protein typically required to generate membrane curvatures such as caveolae; and CHC, a basic component required for clathrin-coated pits and vesicles. Cav-1 and CHC facilitate caveolae- and clathrin-mediated endocytosis, respectively. Confocal microscopy images showed that both CAV-1 (green) and CHC (magenta) accumulated around PS NNs in GPE86 cells (Figure 6e), with stronger CAV-1 accumulation than CHC around the PS NNs; both were distributed throughout the cells on flat PS control (Figure S15a). GPE86 cells on SU8, and PDMS NNs revealed similar accumulation of CAV-1 and CHC (Figure S16a,c), but the aggregation pattern on PDMS NNs were less ordered than for SU8 or PS NNs, due to the major deflection of low stiffness PDMS NNs as shown earlier. Both CAV-1 and CHC distributed throughout the cells on flat SU8, and PDMS (Figure S16b,d). CAV-1 and CHC aggregation around NNs was reported in recent studies using Si and quartz NNs.[2b,30,42] Our results indicate that polymeric NN-mediated endocytosis in GPE86 cells involves both CAV-1 and CHC, but is primarily governed by CAV-1.

There was no significant aggregation of CAV-1 and CHC in L1.2 cells on PS NNs, flat PS, SU8 NNs or flat SU8 control (Figure 6f, S15b, S16e, and S16f, respectively). The

lack of CAV-1 and CHC accumulation in L1.2 cells on polymeric NNs, in particular PS NNs, concurred with our FIB-SEM and TEM imaging, which showed less membrane deformation than for GPE86 cells without invaginations.

By combining FIB-SEM, TEM and confocal microscopy, our results show that polymeric NNs, in particular PS and PDMS NNs, can induce membrane curvatures, especially in GPE86 cells. This, in turn, facilitates formation of endocytic pits such as clathrin-coated pits and caveolae that are recruited to focal adhesion complex sites[66]— formation that has also been reported in other NN studies.[2b,30,42] Enhanced activation of endocytic pathways plays a key role in the increased uptake of biomolecules, in particular the mRNA delivery into GPE86 cells. But a lack of endocytic pits and endocytosis-associated proteins (CAV-1 and CHC) might reduce the efficiency of intracellular delivery efficiency in L1.2 cells. Focal adhesions are active sites for actin polymerization, with reports that endocytosis is likely initiated by the recruitment of its components to these adhesive sites.[66-67] We hypothesize that the absence of focal adhesion formation may be a key reason that endocytic pits and endocytosis component accumulation is not observed in L1.2 cells.

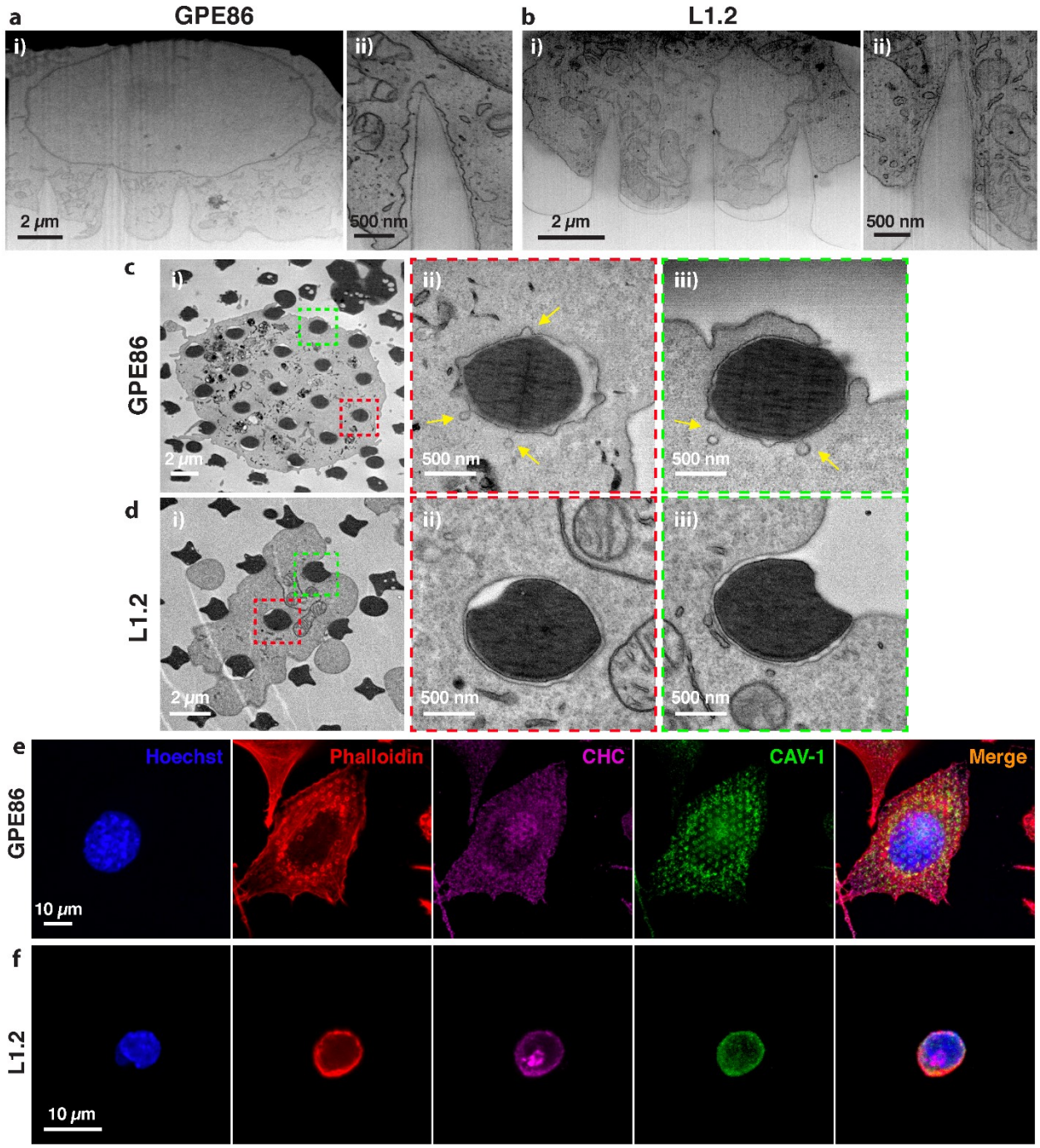

Figure 6. Cellular deformation and endocytosis induced by PS NNs. SEM images after vertical FIB milling, showing (a) GPE86 cells and (b) L1.2 cells interacting with PS NNs with (i) overview and (ii) selected enlarged view of the cell–NN interface after 6 h culture. TEM images showing longitudinally cut views of interfacial interactions of (c) GPE86 cells and (d) L1.2 cells with PS NNs, with (i) overview and (ii,iii) the enlarged views of red and green insets. Yellow arrows indicate endocytic pits and vesicles formed in proximity to NNs.

(e–f) Confocal microscopy images of (e) GPE86 cells cultured 6 h on PS NNs, and (f) L1.2 cells cultured 6 h on PS NNs. Cells were fixed and stained with Hoechst 33342 (blue), phalloidin (red), anti-clathrin heavy chain (CHC, magenta), and anti-caveolin 1 (CAV-1, green) to reveal nucleus, F-actin, and distribution of endocytosis-associated clathrin and caveolae, respectively.

3. Conclusion

The study used vertically aligned polymeric PS, SU8, and PDMS NNs to probe cell–NN interfacial interactions of adherent (GPE86) and suspension (L1.2) cells, and to achieve intracellular delivery with minimum cell perturbation. These polymeric NNs, replicated from one Si master by replica molding and NIL, have the same geometry but different stiffnesses; this allows us to decouple the two parameters to focus on the effect of NNs' stiffness on cell behavior. Such NN platforms, made of low-stiffness PDMS or medium-stiffness PS and SU8, demonstrate cytocompatibility and the capability to mediate intracellular delivery. All the three types of NNs had no short-term impact on viability, apoptosis, and migration of GPE86 and L1.2 cells; and both cell types maintained the ability to proliferate, without significant difference between each polymeric NN type, despite the variance in stiffness. We demonstrate the capacity for polymeric NN-mediated intracellular delivery by transfecting GPE86 and L1.2 cells with Cy5-GFP-mRNA; this yielded similar transfection efficiencies of 26.8±3.5%, 33.2±7.4%, and 30.1±4.1% on GPE86 cells by PS, SU8, and PDMS NNs, respectively, indicating the independence on NN stiffness. We also explored the mechanisms behind polymeric NN-mediated intracellular delivery, using FIB-SEM, TEM, and immunofluorescence imaging; the combined results revealed that enhanced endocytosis (mediated by caveolae and clathrin) is one of the likely delivery mechanisms, especially in

GPE86 cells. There was no prominent accumulation of endocytosis-associated elements or pits at the L1.2 cell–NN interface, resulting lower transfection efficiency compared to GPE86 cells. Our findings demonstrate that polymeric NNs are ideal for decoupling the influences of stiffness from topography on cellular behavior, and for precisely manipulating cellular processes such as intracellular delivery. This significantly broadens the range of controlled cellular manipulation for which relatively low-cost, easy-to-fabricate, and high-throughput polymeric NNs can be used, presenting opportunities for novel integration of nanostructures into traditional polymeric cell cultureware.

4. Experimental Section/Methods

Preparation of Si NN arrays: Flat silicon (Si) wafers (3", p-type, 3 – 6 Ωcm, <100>, Siltronix, France) were cleaned by Piranha solution for 15 minutes to remove any organic contaminants, rinsed with deionized water and dried under nitrogen jet. A close-packed monolayer of PS nanospheres (Polybead microspheres solutions, 3 μm in diameter, 2.5% w/v in water) was deposited over the silicon wafer by convective assembly. The sample was then inserted into Plasmalab 100 ICP380 deep reactive ion etcher (Oxford Instruments) for etching. Shrinkage of the nanospheres by oxygen plasma etching was performed using an inductively-coupled plasma (ICP) power of 500 W and bias power of 50 W over 15 minutes. The shrunken polystyrene nanospheres served as a mask for the subsequent silicon etching in two consecutive steps: 1. Bosch process, including an alternative cycle of passivation and etching steps to obtain cylindrically shaped Si NNs. During the passivation step (8 s), 150 sccm of C_4F_8 and 3 sccm of SF_6 was used with 1500 W ICP power and 5 W bias power. As for the etching step (8 s), 150 sccm of C_4F_8 and 3 sccm of SF_6 was used with 2000 W ICP power and 20 W bias power. 25 loops of the Bosch process were used to create Si NNs of 3.5

μm height. PS nanospheres were then removed by sonicating samples in acetone for 30 s, rinsed by deionized water and dried under a nitrogen gas jet. 2. Pseudo-Bosch process involved etching the sample in an environment with 100 sccm of SF_6 and 40 sccm C_4F_8 at pressure of 10 mTorr, 1500 W ICP power and 50 W bias power for 110 s to obtain a conically shaped Si NN profile.

Preparation of negative mold: The Si NN master was rinsed with acetone, followed by isopropanol, and then dried under a nitrogen gas jet. The master was placed in an air plasma cleaner for 5 minutes before 0.5 h vapor phase deposition of an anti-adhesive layer of trichloro(1H,1H,2H,2H-perfluoro-octyl)silane (Sigma Aldrich) under vacuum to assist the release of the final negative mold. Hard PDMS solution consisting of 0.9 g of VDT, 6.2 μL of SIP, 12.5 μL of SIT and 350 μL of HMMS (Gelest) was mixed and spin coated onto the Si NN template with 500 rpm for 3 s then 3000 rpm for 1 minutes. The sample was placed under vacuum for 5 minutes before being partially cured at 65 °C in an oven for 30 minutes. The sample was removed from the oven and a layer of PDMS (Sylgard 184, Sigma Aldrich) backing with 1:10 ratio was coated on top of the hard PDMS layer and further cured at 60 °C in an oven for 2 h. The PDMS negative mold was released from the Si NN template upon curing and coated with the same anti-adhesive layer for 2 h before the preparation of polymeric NNs.

Preparation of polymeric NN: Nanonex NX-B200 was used to fabricate both PS and SU8 NNs. PS NN fabrication: Untreated cell cultureware PS (Corning) was prepared by rinsing with isopropanol and deionized water. The substrate was then dried with nitrogen gas. The PDMS negative mold was pressed on the PS substrate (with a Si wafer support backing) and placed in between two Si films on a sample holder. 1 minutes of pump time with 40 PSI pressure at 250 °C were set as the pre-imprint parameters. The PS substrate was then

imprinted with 85 PSI at 220 °C for 5 minutes. The mold was held at a constant pressure until the sample temperature dropped below 70 °C. The PDMS mold was removed to obtain PS NNs. SU8 NN fabrication: A glass slide was first rinsed by acetone, isopropanol and deionized water, followed by drying under a stream of nitrogen gas. The glass substrate was then cleaned in a plasma cleaner for 5 minutes prior to NIL. Next, 5 µL of SU8 (class 2002, MicroChem) was placed on the glass substrate and pressed by the negative mold. 5 minutes of pumping time with 75 PSI at 85 °C were set as the pre-imprint parameters. The sample was imprinted at 75 PSI with 85 °C for 5 minutes under vacuum, followed by 2 minutes of UV curing. The PDMS mold was removed to obtain SU8 NNs. PDMS NN fabrication: A glass slide was first rinsed by acetone, isopropanol and deionized water, followed by drying under a stream of nitrogen gas. The glass substrate was then cleaned in a plasma cleaner for 5 minutes prior spin-coated with PDMS (Sylgard 184, Sigma Aldrich) of 1:10 ratio. The negative mold was then placed onto the PDMS coated glass substrate and degas in vacuum under room temperature (RT) for 1 h. The sample was then further cured at 65 °C in an oven for 2 h. The PDMS mold was removed to obtain PDMS NNs.

In situ SEM nanoindentation: Nanoindentation on the flat substrates was performed with a Hysitron TI 950 TriboIndenter equipped with a Berkovich tip, while indentation of NNs was performed with a Hysitron PI 85 Picoindenter equipped with a 10 µm diameter flat punch tip. Indentation with the PI 85 was performed alongside *in situ* SEM imaging. 500 µN – 5000 µN indentation force was applied to the substrates and their Young's moduli were calculated from the plotted stress strain curves.

Surface functionalization of polymeric NNs: Substrates were rinsed with isopropanol and dried by nitrogen gas. Following this, substrates were coated with 10 µL of PDL (Sigma-Aldrich) at a concentration of 167 µg mL^{-1} in deionized water under vacuum for 5 minutes.

The substrates were then transferred and incubated at 4 °C overnight. Excessive PDL solution was aspirated and the substrate placed under UV sterilization in a laminar flow cabinet for 30 minutes before nucleic acid loading.

Loading of mRNA onto polymeric NNs: 12 μL of Cy5-GFP-mRNA (200 μg μL^{-1}, Trilink Biotechnologies) was placed on the PDL-coated substrates and allowed to stand 1 h before contacting with cells. Excess mRNA was removed from the substrates before seeding cells.

Cell culture: Two types of cell lines were used in the experiments: GPE86 (ATCC, mouse embryonic fibroblasts) and L1.2 (ATCC, mouse B cells). GPE86 cells were grown and maintained in complete Dulbecco's modified Eagle's medium (DMEM (Gibco), supplemented with 10% fetal bovine serum (FBS, Gibco), 1 X 10^{-3} M sodium pyruvate, 2 X 10^{-3} M L-glutamine, 100 U mL^{-1} penicillin, and 100 μg mL^{-1} streptomycin (Gibco). L1.2 cells were grown and maintained in complete RPMI (RPMI-1640 (Gibco), consisting of 10% FBS, 10 × 10^{-3} M 4-(2-hydroxyethyl)-1-piperazineethanesulfonic acid, 1 × nonessential amino acids solution (Gibco), 1 × 10^{-3} M sodium pyruvate, 2 × 10^{-3} M L-glutamine, 100 U mL^{-1} penicillin, 100 μg mL^{-1} streptomycin, and 55 × 10^{-6} M 2-mercaptoethanol (Gibco)). Cell densities of 0.1 and 0.2 million cells mL^{-1} were used for seeding GPE86 and L1.2 cells, respectively. All cells were seeded with centrifugal force of 250 g at 32 °C for 15 minutes, and were incubated at 37 °C with 5% CO_2.

Cell fixation and fluorescence staining: Cells grown on the substrates were washed with Dulbecco's phosphate buffered saline (DPBS) and then fixed in a solution of 4% paraformaldehyde (Electron Microscopy Sciences) for 10 minutes, followed by permeabilization with 0.1% Triton X-100 (Sigma-Aldrich) in DPBS for 5 minutes at RT and washing three times with DPBS. Cells were blocked with 1% w/v bovine serum albumin

(BSA, Sigma-Aldrich) solution for 1 h at RT and washed three times with DPBS. For primary antibody staining, cells were stained with Hoechst (Hoechst 33342, Sigma-Aldrich), Alexa Fluor 568 Phalloidin (Life Technologies), anti-vinculin monoclonal antibody (rabbit, Sigma-Aldrich), anti-β-integrin monoclonal antibody (mouse, Invitrogen), anti-caveolin-1 polyclonal antibody (rabbit, Abcam), and anti-clathrin heavy chain monoclonal antibody (mouse, Life Technologies), for 45 minutes at RT. After washing three times with DPBS, cells were then further stained with secondary antibodies, Alexa Fluor 488 chicken anti-rabbit IgG (Life Technologies) and Alexa Fluor 647 goat anti-mouse IgG (Life Technologies), for 30 minutes, RT. Cells were washed three times with DPBS and left in DPBS for laser scanning confocal microscopy imaging.

Laser scanning confocal microscopy: A Nikon A1R confocal laser scanning microscope system and Leica Stellaris 5 were used for fluorescence imaging. Hoechst, FDA, PI, Cy5, GFP, mCherry, Alexa Fluor 488 chicken anti-rabbit IgG, Alexa Fluor 568 Phalloidin, and Alexa Fluor 647 goat anti-mouse IgG were excited at 340, 450, 493, 650, 488, 587, 488, 578, and 647 nm, with emission at 510, 515, 636, 670, 509, 610, 520, 600, and 670 nm, respectively. A 20 X dry objective lens, 60 X water immersed objective lens and 60 X oil immersed objective lens were used for observation and more than 3 different locations were selected for 3 sample. Images were analyzed using the Nikon NIS-Elements Advanced Research software and Leica Application Suite X provided by the manufacturers.

Live cell microscopy for migration study: mCherry GPE86 cells (cell density 0.1 million cells mL^{-1}) and L1.2 cells (0.2 million cells mL^{-1}) were seeded onto substrates in a 24-well plate, followed by centrifugation at 250 g, 32 °C, 15 minutes and incubated at 37 °C and 5% CO_2 for 1 h. After incubation, cells were stained using Hoechst for 10 minutes and transferred to a Nunc glass bottom dish (Thermo Fisher Scientific) with fresh complete

DMEM (for GPE86) and RPMI (for L1.2). The sample was then placed in the portable incubation chamber provided by the manufacturer, at 37 °C and 5% CO_2. mCherry was excited using the 587 nm laser with low intensity, to avoid phototoxicity that might induce cell death, and detected at 610 nm. This was observed at magnification of 20X objective lens. Confocal images were taken every 10 minutes over 12 h. Live cell images were analyzed using Leica Application Suite X Tracking Module.

Sample preparation for SEM imaging: Cells interfaced with polymeric NNs and flat substrates were rinsed with 0.1 M sodium cacodylate buffer (Electron Microscopy Sciences) and fixed with 2.5% glutaraldehyde (Electron Microscopy Sciences) in 0.1 M sodium cacodylate 4 °C for 1 h. Following this, substrates were washed (3 × 5 minutes) with chilled 0.1 M sodium cacodylate buffer and gradually dehydrated with increasing concentrations of ethanol: 50%, 70%, 90% (1 × 10 minutes), and 100% (2 × 10 minutes) at RT, and were finally critical point dried (CPD 030 Critical Point Dryer, BAL-TEC). Substrates were then mounted on SEM stubs and sputter-coated with a 10 nm layer of gold in order to increase their conductivity for SEM imaging.

Intracellular compartments staining and FIB-SEM sample preparation: Heavy metal staining and resin embedding were used as the sample preparation method. Samples were rinsed with 0.1 M sodium cacodylate buffer (Electron Microscopy Sciences) and fixed with 2.5% glutaraldehyde (Electron Microscopy Sciences) in the same buffer at 4 °C for 1 h. Following this, the samples were washed (3 × 5 minutes) with chilled 0.1 M sodium cacodylate buffer and quenched with chilled 20×10^{-3} M glycine solution (Sigma-Aldrich) in the same buffer for 20 minutes. After repeating the washing step, samples were post fixed by combining equal volumes of 4% aqueous osmium tetroxide with 2% potassium ferrocyanide (UNIVAR) in 0.2 M sodium cacodylate buffer on ice for 1 h. Samples were re-washed (3 × 5

minutes) with chilled buffer and incubated with 1% tannic acid (BDH) in deionized water at RT for 20 minutes. After rinsing with sodium cacodylate buffer (2 × 5 minutes), samples were further incubated with 2% aqueous osmium tetroxide at RT for 30 minutes. Samples were washed (2 × 5 minutes) with deionized water and incubated with syringe-filtered 4% aqueous uranyl acetate (UNIVAR) at 4 °C overnight. Samples were washed (3 × 5 minutes) with chilled deionized water and gradually dehydrated with increasing concentrations of ethanol: 10%, 30%, 50%, 70%, 90%, and 100% (1 × 7 minutes) at RT. An Epon 812 resin 20 mL solution was prepared by initially mixing 12.2 g of DDSA (dodecenyl succinic anhydride specially distilled, Electron Microscopy Sciences), 4.4 g of Araldite (GY 502, Electron Microscopy Sciences), and 6.2 g of Procure 812 (EMBED 812 RESIN) using a mechanical stirrer. Once the solution was uniformly mixed, 0.8 mL of N-benzyldimethylamine (BDMA, Electron Microscopy Sciences) was added while stirring. Samples were infiltrated with increasing concentrations of the freshly prepared resin solution in 100% ethanol at RT and in a sealed container using the following ratios: 1:3 (3 h), 1:2 (3 h), 1:1 (overnight), 2:1 (3 h), 3:1 (3 h). Following this, samples were finally infiltrated with 100% resin solution overnight. The excess resin was drained away by mounting the samples vertically for 1 h and samples were left for polymerization at 60 °C in an oven for 48 h. The sample were sputtered coated with 10 nm Au prior sectioning and imaging.

TEM sample preparation: Step 1: PDL coating. 10 µL of PDL solution (167 ng μL^{-1}) (Sigma Aldrich) was drop casted onto PS NNs and placed in a desiccator for 10 minutes. Following this, samples were left at 4 °C overnight. Step 2: Cell Seeding. GPE86 and L1.2 cells were seeded at a density of 0.1 and 0.2 million cells mL^{-1}, respectively, onto the PS substrates followed by centrifugation at 250 g, 32 °C, 15 minutes. Substrates carrying cells were incubated at 37 °C with 5% CO_2 for 6 h. Step 3: Fixation, Heavy Metal Staining, Dehydration and Resin Embedding. Samples were rinsed with 0.1 M sodium cacodylate

buffer (Electron Microscopy Sciences) and fixed with 2.5% glutaraldehyde (Electron Microscopy Sciences) in the same buffer at 4 °C overnight. Following this, samples were washed (3 × 5 minutes) with chilled 0.1 M sodium cacodylate buffer (Electron Microscopy Sciences) and quenched with chilled 20 mM glycine solution (Sigma-Aldrich) in the same buffer for 20 minutes. After repeating the washing step, samples were post-fixed by combining equal volumes of 4% aqueous osmium tetroxide with 2% potassium ferrocyanide (UNIVAR) in 0.2 M sodium cacodylate buffer on ice for 1 h. Samples were then washed again (3 × 5 minutes) with chilled buffer and incubated with 1% tannic acid (BDH) in deionized water at RT for 20 minutes. After rinsing with buffer (2 × 5 minutes) samples were further incubated with 2% aqueous osmium tetroxide at RT for 30 minutes. Following this, samples were washed (2 × 5 minutes) with deionized water and incubated with syringe-filtered 1% aqueous uranyl acetate (UNIVAR) at 4 ˚C overnight. Samples were then washed (3 × 5 minutes) with chilled deionized water and gradually dehydrated with increasing concentrations of ethanol; 10%, 30%, 50%, 70%, 90% and 100% (1 × 7 minutes) at RT. An Epon 812 resin 20 mL solution was prepared by initially mixing 12.2 g of DDSA (Dodecenyl Succinic Anhydride Specially Distilled 13710, Electron Microscopy Sciences), 4.4 g of Araldite (GY 502 10900, Electron Microscopy Sciences) and 6.2 g of Procure 812 (EMBED 812 RESIN 14900) using a mechanical stirrer. Once the solution was uniformly mixed, 0.8 mL of BDMA (Electron Microscopy Sciences) was added to it while stirring. Samples were then infiltrated with increasing concentrations of the freshly prepared resin solution in 100% ethanol at RT and in a sealed container using the following ratios: 1:3 (3 h), 1:2 (3 h), 1:1 (overnight), 2:1 (3 h), 3:1 (3 h). Following this, samples were finally infiltrated with 100% resin solution overnight. The excess resin was drained away by mounting the samples vertically for 1 h. Samples were then placed face down on resin-filled micromolds (ProSciTech) and left for polymerization at 60 ˚C for 48 h. After polymerization was

completed, substrates were detached using tweezers and resin blocks were released from the micromolds. Step 4: Resin Block Trimming and Microtome Sectioning. Each resin block was fixed in a metal specimen holder for ultramicrotomes and inspected under the microscope for the localization of the region of interest (ROI). Following this, the resin block was manually trimmed at the sides using a double-edged razor blade so that a pyramid with 45˚ angled sides and square surface (0.5 mm x 0.5 mm) containing the ROI is formed. Thin (70 nm) serial sections of the trimmed resin block were then acquired using an ultra-microtome (Leica Ultracut UCT) equipped with a diamond knife. Sections were collected on TEM grids (ProSciTech, formvar/carbon coated, square 100 mesh).

SEM imaging: A Nova NanoSEM 430 (FEI) was used to image all polymeric NN samples including flat polymeric substrate as well as flat Si and Si NNs. The images were taken at top view or tilted 45° with electron beam acceleration voltage of 5, 10, 15 and 20 kV, with current of 96 nA, while using a secondary electron detector. High resolution images were taken in immersion mode with acceleration voltage of 20 kV and current of 92 nA.

FIB sectioning and imaging: FIB sectioning was performed using a Thermo Fischer Helios Nanolab 600. Prior to FIB sectioning, ion-beam facilitated Pt deposition of ~0.5 µm thickness was performed to protect the area of interest at 30 kV and with 3-5 pA μm^{-2} current density. Rough milling was performed at an acceleration voltage of 30 kV voltage and current ranging between 2.8 – 4.6 nA, and the surface was polished with 30 kV voltage and 0.46 – 2.8 nA. Images were taken using an electron beam acceleration voltage of 5 and 10 kV and current of 86 nA using free field and immersion mode with through-the-lens detector (TLD) operating under secondary electron collection mode, at dwell time of 5 µs and 6144 x 4096 $pixel^2$ resolution. Original images are black-white inverted.

TEM imaging: TEM was performed using a JEOL 1400 Flash operated at 80 kV and images were acquired at different magnifications.

Cell viability assay: All cells were seeded with centrifugal force of 250 g at 32°C for 15 minutes, and were incubated at 37 °C with 5% CO_2 over 6 h. A live-dead staining assay was used to determine the viability of cells on substrates with final concentration of 15 μg mL^{-1} FDA (Sigma-Aldrich) and 5 μg mL^{-1} PI (Sigma-Aldrich) in media for 5 minutes at 37 °C. Samples were rinsed with DPBS after staining and observed using a Stellaris 5 laser scanning confocal microscope (Leica). Three different locations were observed on the surface of each sample at the magnification of 20X objective lens with 3 duplicates for each sample.

Flow cytometry: An LSRIIb flow cytometer (BD) was used to investigate the insertion and transfection efficiency, proliferation, and apoptosis of cells harvested from the substrates.

Flow cytometry insertion and transfection efficiency: To detect the insertion of mRNA and GFP expression, GPE86 and L12 cells were harvested from the substrates loaded with mRNA after 6 h incubation. The excitation/emission wavelengths for Cy5 and GFP on LSRIIb were 678/694, and 488/540 nm, respectively. Proper negative and positive controls were used for the flow cytometry analysis. Compensation was done to avoid fluorescence leakage between different channels.

Apoptosis Assay: A Caspase- Glo 3/7 kit (Promega) was used for apoptosis detection. Target cell density was 0.1 million cells mL^{-1} of GPE86 and 0.2 million cells mL^{-1} of L1.2 cells in 96 well plate. Cells were seeded to the polymeric substrates and centrifugated at 250 g, 32 °C for 15 minutes. A 1:1 ratio of caspase-Glo 3/7 reagent volume to sample volume was used. At time points of 2, 6, 24 h, the reagent is added to the cell culture and incubated at RT for 2 h on a shaker at 55 rpm, isolated from light. The positive control was cells treated with 200 μg mL^{-1} propranolol, the negative control was cell culture without reagent, and blank

sample was media with reagent. Luminescence reading was performed on a plate reader (Synergy H4, BioTek) and the result was normalized to a blank sample (cell culture medium without cells).

Flow cytometry proliferation assay: 0.1 million cells mL^{-1} of GPE86, and 0.2 million cells mL^{-1} of L1.2 cells were stained with 5 x 10^{-6} M CellTrace Violet (CTV) reagent (Invitrogen), seeded onto substrates in a 24-well plate and centrifugated at 250 g, 32 °C, 15 minutes. Substrates carrying cells were then transferred to a new plate with fresh media after 1 h and further incubated at 37 °C with 5 % CO_2 for a total of 6 h. Cells were then harvested from the substrate as described above and placed back in fresh media culture. At time points of 0, 6, 24, and 48 h, cells were resuspended in FACS buffer (1 x DPBS containing 1 % BSA, 2 x 10^{-3} M ethylenediaminetetraacetic acid (EDTA), and 0.1 % sodium azide) and cell proliferation was determined by measuring the fluorescence intensity of CTV using the LSRIIb. 405 nm excitation and a 460 nm bandpass emission filter was used. Unstained cell and CTV-stained cells fixed in FACS buffer after 6 h incubation served as negative and positive controls, respectively.

Polymeric NN-mediated cell transfection: 0.1 million cells mL^{-1} of GPE86, 0.2 million cells mL^{-1} of L1.2 were seeded onto PDL-coated and cargo-loaded substrates described above in a 24-well plate, in 500 µL Opti-MEM (Gibco), followed by centrifugation at 250 G, 32 °C, 15 minutes. The samples were then incubated for 6 h at 37 °C in a humidified 5% CO_2 atmosphere (samples were transferred to new wells with fresh media 2 h after centrifugation). The transfected cells were then detached from the substrates using 0.25% Trypsin/EDTA (Gibco) for adherent cells, or by gently pipetting for suspension cells. The cells were resuspended in FACs media for flow cytometry analysis.

Data processing and statistical analysis: Fluorescence microscopy and SEM images were processed and analyzed by Leica Application Suite X (Leica), NIS-Element (Nikon) and FIJI. Flow cytometry data were analyzed with FlowJo. Prism GraphPad 7 were used for all statistical analyses. One way/two-way ANOVA were used for the analyses. Values are represented as mean and mean ± standard deviation.

Supporting Information

Supporting Information is available from the Wiley Online Library or from the author.

Acknowledgements

H.Y. and Y.C. contributed equally to this work. This work was supported by ARC CPPT, Motherson Innovation, and CSIRO Manufacturing, and was in part funded by the Australian government (ARC DECRA project number: DE170100021). This work was performed in part at the Melbourne Centre for Nanofabrication (MCN) in the Victorian Node of the Australian National Fabrication Facility (ANFF) and Swinburne Nanolab.

Received: ((will be filled in by the editorial staff))
Revised: ((will be filled in by the editorial staff))
Published online: ((will be filled in by the editorial staff))

References

[1] a) S. G. Higgins, M. Becce, A. Belessiotis-Richards, H. Seong, J. E. Sero, M. M. Stevens, *Adv. Mater.* **2020**, *32*, 1903862; b) E. Lestrell, F. Patolsky, N. H. Voelcker, R. Elnathan, *Mater. Today* **2020**, *33*, 87; c) A. F. McGuire, F. Santoro, B. Cui, *Ann. Rev. Anal. Chem.* **2018**, *11*, 101; d) B. Tian, S. Xu, J. A. Rogers, S. Cestellos-Blanco, P. Yang, J. L. Carvalho-de-Souza, F. Bezanilla, J. Liu, Z. Bao, M. Hjort, Y. Cao, N. Melosh, G. Lanzani, F. Benfenati, G. Galli, F. Gygi, R. Kautz, A. A. Gorodetsky, S. S. Kim, T. K. Lu, P. Anikeeva, M. Cifra, O. Krivosudský, D. Havelka, Y. Jiang, *Phys. Biol.* **2018**, *15*, 031002.

[2] a) C. S. Hansel, S. W. Crowder, S. Cooper, S. Gopal, M. João Pardelha da Cruz, L. de Oliveira Martins, D. Keller, S. Rothery, M. Becce, A. E. G. Cass, C. Bakal, C. Chiappini, M. M. Stevens, *ACS Nano* **2019**, *13*, 2913; b) S. Gopal, C. Chiappini, J. Penders, V. Leonardo, H. Seong, S. Rothery, Y. Korchev, A. Shevchuk, M. M. Stevens, *Adv. Mater.* **2019**, *31*, 1806788; c) R. Elnathan, B. Delalat, D. Brodoceanu, H. Alhmoud, F. J. Harding, K. Buehler, A. Nelson, L. Isa, T. Kraus, N. H. Voelcker, *Adv. Funct. Mater.* **2015**, *25*, 7215.

[3] a) J. J. VanDersarl, A. M. Xu, N. A. Melosh, *Nano Letters* **2012**, *12*, 3881; b) L. Schmiderer, A. Subramaniam, K. Žemaitis, A. Bäckström, D. Yudovich, S. Soboleva, R. Galeev, C. N. Prinz, J. Larsson, M. Hjort, *PNAS* **2020**, *117*, 21267.
[4] Y. Chen, S. Aslanoglou, T. Murayama, G. Gervinskas, L. I. Fitzgerald, S. Sriram, J. Tian, A. P. R. Johnston, Y. Morikawa, K. Suu, R. Elnathan, N. H. Voelcker, *Adv. Mater.* **2020**, *32*, 2000036.
[5] a) A.-R. Shokouhi, S. Aslanoglou, D. Nisbet, N. H. Voelcker, R. Elnathan, *Mater. Horiz.* **2020**, *7*, 2810; b) Z. Liu, J. Nie, B. Miao, J. Li, Y. Cui, S. Wang, X. Zhang, G. Zhao, Y. Deng, Y. Wu, Z. Li, L. Li, Z. L. Wang, *Adv. Mater.* **2019**, *31*, 1807795; c) G. He, J. Feng, A. Zhang, L. Zhou, R. Wen, J. Wu, C. Yang, J. Yang, C. Li, D. Chen, J. Wang, N. Hu, X. Xie, *Nano Lett.* **2019**, *19*, 7201; d) R. Wen, A.-h. Zhang, D. Liu, J. Feng, J. Yang, D. Xia, J. Wang, C. Li, T. Zhang, N. Hu, T. Hang, G. He, X. Xie, *ACS App. Mater. Interfaces* **2019**, *11*, 43936.
[6] a) R. Elnathan, M. Kwiat, F. Patolsky, N. H. Voelcker, *Nano Today* **2014**, *9*, 172; b) X. Li, L. Matino, W. Zhang, L. Klausen, A. F. McGuire, C. Lubrano, W. Zhao, F. Santoro, B. Cui, *Nat. Protoc.* **2019**, *14*, 1772; c) M. Kwak, L. Han, J. J. Chen, R. Fan, *Small* **2015**, *11*, 5600; d) A. Tay, N. Melosh, *Acc. Chem. Res.* **2019**, *52*, 2462; e) C. S. Hansel, M. N. Holme, S. Gopal, M. M. Stevens, *Biomater.* **2020**, *226*, 119406.
[7] M. P. Stewart, R. Langer, K. F. Jensen, *Chem. Rev.* **2018**, *118*, 7409.
[8] a) M. Á. Fernández-Rodríguez, R. Elnathan, R. Ditcovski, F. Grillo, G. M. Conley, F. Timpu, A. Rauh, K. Geisel, T. Ellenbogen, R. Grange, F. Scheffold, M. Karg, W. Richtering, N. H. Voelcker, L. Isa, *Nanoscale* **2018**, *10*, 22189; b) J.-A. Huang, V. Caprettini, Y. Zhao, G. Melle, N. Maccaferri, L. Deleye, X. Zambrana-Puyalto, M. Ardini, F. Tantussi, M. Dipalo, F. De Angelis, *Nano Lett.* **2019**, *19*, 722.
[9] C. Chiappini, E. De Rosa, J. O. Martinez, X. Liu, J. Steele, M. M. Stevens, E. Tasciotti, *Nat. Mater.* **2015**, *14*, 532.
[10] a) H. Seong, S. G. Higgins, J. Penders, J. P. K. Armstrong, S. W. Crowder, A. C. Moore, J. E. Sero, M. Becce, M. M. Stevens, *ACS Nano* **2020**, *14*, 5371; b) A. M. Xu, S. A. Kim, D. S. Wang, A. Aalipour, N. A. Melosh, *Lab Chip* **2016**, *16*, 2434; c) A. K. Shalek, J. T. Gaublomme, L. Wang, N. Yosef, N. Chevrier, M. S. Andersen, J. T. Robinson, N. Pochet, D. Neuberg, R. S. Gertner, I. Amit, J. R. Brown, N. Hacohen, A. Regev, C. J. Wu, H. Park, *Nano Lett.* **2012**, *12*, 6498; d) Y. Cao, H. Chen, R. Qiu, M. Hanna, E. Ma, M. Hjort, A. Zhang, R. S. Lewis, J. C. Wu, N. A. Melosh, *Sci. Adv.* **2018**, *4*, eaat8131; e) F. J. Harding, S. Surdo, B. Delalat, C. Cozzi, R. Elnathan, S. Gronthos, N. H. Voelcker, G. Barillaro, *ACS Appl. Mater. Interfaces* **2016**, *8*, 29197.
[11] a) H. Persson, J. P. Beech, L. Samuelson, S. Oredsson, C. N. Prinz, J. O. Tegenfeldt, *Nano Res.* **2012**, *5*, 190; b) P. Yang, S.-J. Chou, J. Li, W. Hui, W. Liu, N. Sun, R. Y. Zhang, Y. Zhu, M.-L. Tsai, H. I. Lai, M. Smalley, X. Zhang, J. Chen, Z. Romero, D. Liu, Z. Ke, C. Zou, C.-F. Lee, S. J. Jonas, Q. Ban, P. S. Weiss, D. B. Kohn, K. Chen, S.-H. Chiou, H.-R. Tseng, *Sci. Adv.* **2020**, *6*, eabb7107.
[12] a) S. Choi, H. Kim, S. Y. Kim, E. G. Yang, *Nanoscale* **2016**, *8*, 11380; b) S. G. Higgins, M. M. Stevens, *Science* **2017**, *356*, 379.
[13] J. Abbott, T. Ye, D. Ham, H. Park, *Acc.Chem. Res.* **2018**, *51*, 600.
[14] Y. Chen, J. Wang, X. Li, N. Hu, N. H. Voelcker, X. Xie, R. Elnathan, *Adv. Mater.* **2020**, *32*, 2001668.
[15] a) C. Chiappini, *ACS Sens.* **2017**, *2*, 1086; b) R. Kawamura, M. Miyazaki, K. Shimizu, Y. Matsumoto, Y. R. Silberberg, R. R. Sathuluri, M. Iijima, S. i. Kuroda, F. Iwata, T. Kobayashi, C. Nakamura, *Nano Lett.* **2017**, *17*, 7117; c) Y. Chen, M. Alba, T. Tieu, Z. Tong, R.S. Minhas, D. Rudd, N.H. Voelcker, A. Cifuentes-Rius, R. Elnathan, *Adv. Nanobiomed Res.* **2021**, 2100002.
[16] a) H.-Y. Lou, W. Zhao, Y. Zeng, B. Cui, *Acc. Chem. Res.* **2018**, *51*, 1046; b) H.-Y. Lou, W. Zhao, X. Li, L. Duan, A. Powers, M. Akamatsu, F. Santoro, A. F. McGuire, Y. Cui, D. G. Drubin, B. Cui, *PNAS* **2019**, *116*, 23143.
[17] G. He, N. Hu, A. M. Xu, X. Li, Y. Zhao, X. Xie, *Adv. Funct. Mater.* **2020**, *30*, 1909890.
[18] a) M. Ermis, E. Antmen, V. Hasirci, *Bioact. Mater.* **2018**, *3*, 355; b) B. M. Rey, R. Elnathan, R. Ditcovski, K. Geisel, M. Zanini, M.-A. Fernandez-Rodriguez, V. V. Naik, A. Frutiger, W.

Richtering, T. Ellenbogen, N. H. Voelcker, L. Isa, *Nano Lett.* **2016**, *16*, 157; c) C. Chiappini, in *Handbook of Porous Silicon*, (Ed: L. Canham), Springer International Publishing, Cham, Switzerland **2018**, p. 185; d) D. Brodoceanu, H. Z. Alhmoud, R. Elnathan, B. Delalat, N. H. Voelcker, T. Kraus, *Nanotechnol.* **2016,** *27*, 275301; e) R. Elnathan, L. Isa, D. Brodoceanu, A. Nelson, F. J. Harding, B. Delalat, T. Kraus, N. H. Voelcker, *ACS Appl. Mater. Interfaces* **2015**, *7*, 23717; f) L. Scheidegger, M. A. Fernández-Rodríguez, K. Geisel, M. Zanini, R. Elnathan, W. Richtering, L. Isa, *Phys. Chem. Chem. Phys.* **2017***, 19*, 8671; g) D. Brodoceanu, R. Elnathan, B. Prieto-Simón, B. Delalat, T. Guinan, E. Kroner, N. H. Voelcker, T. Kraus, *ACS Appl. Mater. Interfaces* **2015***, 7*, 1160.

[19] a) H. Alhmoud, D. Brodoceanu, R. Elnathan, T. Kraus, N. H. Voelcker, *Prog.Mater. Sci.* **2019**, *116*, 100636; b) H. Kim, H. Jang, B. Kim, M. K. Kim, D. S. Wie, H. S. Lee, D. R. Kim, C. H. Lee, *Sci. Adv.* **2018**, *4*, eaau6972.

[20] S. Aslanoglou, Y. Chen, V. Oorschot, Z. Trifunovic, E. Hanssen, K. Suu, N. H. Voelcker, R. Elnathan, J. *Am. Chem. Soc.* **2020**, *142*, 15649.

[21] C. Chiappini, C. Almeida, in *Semiconducting Silicon Nanowires for Biomedical Applications*, Woodhead Publishing, (Ed: J. L. Coffer), Woodhead Publishing, Oxford, UK **2014**, p. 144.

[22] H. J. Han, J. W. Jeong, S. R. Yang, C. Kim, H. G. Yoo, J.-B. Yoon, J. H. Park, K. J. Lee, T.-S. Kim, S.-W. Kim, Y. S. Jung, *ACS Nano* **2017**, *11*, 11642.

[23] a) R. Elnathan, A. W. Holle, J. Young, M. A. George, O. Heifler, A. Goychuk, E. Frey, R. Kemkemer, J. P. Spatz, A. Kosloff, F. Patolsky, N. H. Voelcker, *J. Nanobiotechnol.* **2021**, *19*, 51; b) H. Kim, H. S. Lee, Y. Jeon, W. Park, Y. Zhang, B. Kim, H. Jang, B. Xu, Y. Yeo, D. R. Kim, C. H. Lee, *ACS Nano* **2020**, *14*, 7227; c) H. Kim, H. Jang, B. Kim, M. K. Kim, D. S. Wie, H. S. Lee, D. R. Kim, C. H. Lee, *Sci. Adv.* **2018**, *4*, eaau6972.

[24] a) Y. Zhang, C.-W. Lo, J. A. Taylor, S. Yang, *Langmuir* **2006**, *22*, 8595; b) S. Park, H.-H. Park, K. Sun, Y. Gwon, M. Seong, S. Kim, T.-E. Park, H. Hyun, Y.-H. Choung, J. Kim, H. E. Jeong, *ACS Nano* **2019**, *13*, 11181.

[25] a) K. S. Beckwith, S. P. Cooil, J. W. Wells, P. Sikorski, *Nanoscale* **2015**, *7*, 8438; b) H. Hubbe, E. Mendes, P. E. Boukany, *Micromachines* **2019**, *10*, 225; c) G. Tullii, F. Giona, F. Lodola, S. Bonfadini, C. Bossio, S. Varo, A. Desii, L. Criante, C. Sala, M. Pasini, C. Verpelli, F. Galeotti, M. R. Antognazza, *ACS Appl. Mater. Interfaces* **2019**, *11*, 28125; d) S. De Martino, W. Zhang, L. Klausen, H.-Y. Lou, X. Li, F. S. Alfonso, S. Cavalli, P. A. Netti, F. Santoro, B. Cui, *Nano Lett.* **2020**, *20*, 577.

[26] a) J.-Y. Shiu, L. Aires, Z. Lin, V. Vogel, *Nat. Cell Biol.* **2018**, *20*, 262; b) F. Tamzalit, M. S. Wang, W. Jin, M. Tello-Lafoz, V. Boyko, J. M. Heddleston, C. T. Black, L. C. Kam, M. Huse, *Sci. Immunol.* **2019**, *4*, eaav5445; c) W. Jin, F. Tamzalit, P. K. Chaudhuri, C. T. Black, M. Huse, L. C. Kam, *PNAS* **2019**, *116*, 19835.

[27] a) D. Patil, A. Sharma, S. Aravindan, P. V. Rao, *Micro Nano Lett.* **2019**, *14*, 191; b) J. Valle, S. Burgui, D. Langheinrich, C. Gil, C. Solano, A. Toledo-Arana, R. Helbig, A. Lasagni, I. Lasa, *Macromol. Biosci.* **2015**, *15*, 1060; c) S. Kim, U. T. Jung, S.-K. Kim, J.-H. Lee, H. S. Choi, C.-S. Kim, M. Y. Jeong, *ACS Appl. Mater. Interfaces* **2015**, *7*, 326; d) M. N. Dickson, E. I. Liang, L. A. Rodriguez, N. Vollereaux, A. F. Yee, *Biointerphases* **2015**, *10*, 021010; e) H. Alhmoud, B. Delalat, X. Ceto, R. Elnathan, A. Cavallaro, K. Vasilev, N. H. Voelcker, *RSC Adv.* **2016**, *6,* 65976.

[28] a) Y. Xin, G. Pandraud, L. Otten, Y. Zhang, P. French, *Proc.* **2018**, *2*, 1081; b) K. S. Beckwith, S. Ullmann, J. Vinje, P. Sikorski, *Small* **2019**, *15*, 1902514; c) V. Solis-Tinoco, S. Marquez, T. Quesada-Lopez, F. Villarroya, A. Homs-Corbera, L. M. Lechuga, *Sens. Actuators B* **2019**, *291*, 48.

[29] a) F. Milos, A. Belu, D. Mayer, V. Maybeck, A. Offenhäusser, *Adv. Biol.* **2021**, *5*, 2000248; b) J. Carthew, H. H. Abdelmaksoud, M. Hodgson-Garms, S. Aslanoglou, S. Ghavamian, R. Elnathan, J. P. Spatz, J. Brugger, H. Thissen, N. H. Voelcker, V. J. Cadarso, J. E. Frith, *Adv. Sci.* **2021**, *8*, 2003186; c) S. An, J. Lim, D. Choi, H. Hong, H. W. Kim, S. M. Park, J. W. Rhie, D. S. Kim, *Microelectron. Eng.* **2017**, *174*, 28; d) L. Song, K. Wang, Y. Li, Y. Yang, *Colloids Surf. B*

2016, *148*, 49; e) E. Käpylä, A. Sorkio, S. Teymouri, K. Lahtonen, L. Vuori, M. Valden, H. Skottman, M. Kellomäki, K. Juuti-Uusitalo, *Langmuir* **2014**, *30*, 14555; f) E. Lestrell, C.M. O'Brien, R. Elnathan, N.H. Voelcker, *Adv. Therap.* **2021**, 210061.

[30] Y. Chen, S. Aslanoglou, G. Gervinskas, H. Abdelmaksoud, N. H. Voelcker, R. Elnathan, *Small* **2019**, *15*, 1904819.

[31] K. Mohamed, in *Comprehensive Nanoscience and Nanotechnology (Second Edition)*, Vol. 2 (Eds: D. L. Andrews, R. H. Lipson, T. Nann), Academic Press, Oxford, UK **2019**, p. 357.

[32] a) L. Chen, C. Yan, Z. Zheng, *Mater. Today* **2018**, *21*, 38; b) L. Wang, C. Wang, S. Wu, Y. Fan, X. Li, *Biomater. Sci.* **2020**, *8*, 2714.

[33] a) J. Fu, Y.-K. Wang, M. T. Yang, R. A. Desai, X. Yu, Z. Liu, C. S. Chen, *Nat. Methods* **2010**, *7*, 733; b) Y. Sun, K. M. A. Yong, L. G. Villa-Diaz, X. Zhang, W. Chen, R. Philson, S. Weng, H. Xu, P. H. Krebsbach, J. Fu, *Nat. Mater.* **2014**, *13*, 599.

[34] a) R. J. McMurray, N. Gadegaard, P. M. Tsimbouri, K. V. Burgess, L. E. McNamara, R. Tare, K. Murawski, E. Kingham, R. O. C. Oreffo, M. J. Dalby, *Nat. Mater.* **2011**, *10*, 637; b) T. Tzvetkova-Chevolleau, A. Stéphanou, D. Fuard, J. Ohayon, P. Schiavone, P. Tracqui, *Biomater.* **2008**, *29*, 1541.

[35] a) J. Park, D.-H. Kim, H.-N. Kim, C. J. Wang, M. K. Kwak, E. Hur, K.-Y. Suh, S. S. An, A. Levchenko, *Nat. Mater.* **2016**, *15*, 792; b) L. Trichet, J. Le Digabel, R. J. Hawkins, S. R. K. Vedula, M. Gupta, C. Ribrault, P. Hersen, R. Voituriez, B. Ladoux, *PNAS* **2012**, *109*, 6933.

[36] a) K. Kulangara, J. Yang, M. Chellappan, Y. Yang, K. W. Leong, *PLoS One* **2014**, *9*, e114698; b) J. D. Mih, A. Marinkovic, F. Liu, A. S. Sharif, D. J. Tschumperlin, *J. Cell Sci.* **2012**, *125*, 5974.

[37] A. Bruce, R. Evans, R. Mezan, L. Shi, B. S. Moses, K. H. Martin, L. F. Gibson, Y. Yang, *PLoS One* **2015**, *10*, e0140506.

[38] S.-Y. Chang, *In-Situ* Nanomechanical Testing in Electron Microscopes in *Handbook of Mechanics of Materials*, (Eds: S. Schmauder, C.-S. Chen, K. K. Chawla, N. Chawla, W. Chen, Y. Kagawa), Springer Singapore, Singapore **2018**, p. 1.

[39] Y.-S. Sohn, J. Park, G. Yoon, J. Song, S.-W. Jee, J.-H. Lee, S. Na, T. Kwon, K. Eom, *Nanoscale Res. Lett.* **2009**, *5*, 211.

[40] a) R. Seghir, S. Arscott, *Sens. Actuators. A.* **2015**, 230, 33; b) J. Chang, K.B. Toga, J.D. Paulsen, M. Menon, T.P. Russell, *Macromolecules* **2018**, 51, 6764.

[41] a) Y. Ding, G.K. Xu, G.F. Wang, *Sci. Rep.* **2017**, *7*, 45575; b) N. Gavara, R.S. Chadwick, *Nat. Nanotechnol.* **2012**, *7*, 733; c) Q. Guo, Y. Xia, M. Sandig, J. Yang, *J. Biomech.* **2012**, *45*, 304.

[42] W. Zhao, L. Hanson, H.-Y. Lou, M. Akamatsu, P. D. Chowdary, F. Santoro, J. R. Marks, A. Grassart, D. G. Drubin, Y. Cui, B. Cui, *Nat. Nanotechnol.* **2017**, *12*, 750.

[43] C. Chiappini, J. O. Martinez, E. De Rosa, C. S. Almeida, E. Tasciotti, M. M. Stevens, *ACS Nano* **2015**, *9*, 5500.

[44] M. J. Lerman, J. Lembong, S. Muramoto, G. Gillen, J. P. Fisher, *Tissue Eng. B Rev.* **2018**, *24*, 359.

[45] a) E. M. Harnett, J. Alderman, T. Wood, *Colloids Surf. B* **2007**, *55*, 90; b) A. Blau, *COCIS* **2013**, *18*, 481.

[46] a) K. Yang, K. Jung, E. Ko, J. Kim, K. I. Park, J. Kim, S.-W. Cho, *ACS Appl. Mater. Interfaces* **2013**, *5*, 10529; b) S.-R. Ryoo, Y.-K. Kim, M.-H. Kim, D.-H. Minutes, *ACS Nano* **2010**, *4*, 6587.

[47] P. Atherton, B. Stutchbury, D. Jethwa, C. Ballestrem, *Exp. Cell Res.* **2016**, *343*, 21.

[48] F.-C. Chien, Y.-H. Dai, C. W. Kuo, P. Chen, *Nanotechnol.* **2016**, *27*, 475101.

[49] C. W. Kuo, D.-Y. Chueh, P. Chen, *J. Nanobiotechnol.* **2014**, *12*, 54.

[50] L. R. Motadi, M. S. Choene, N. N. Mthembu, *Sci. Rep.* **2020**, *10*, 12924.

[51] F. Wang, H. Liu, F. Wang, R. Xu, P. Wang, F. Tang, X. Zhang, Z. Zhu, H. Lv, T. Han, *Mol. Med. Rep.* **2018**, *17*, 5213.

[52] N. Van Opdenbosch, M. Lamkanfi, *Immunity* **2019**, *50*, 1352.

[53] N. S. S. Abdul Halim, K. S. Fakiruddin, S. A. Ali, B. H. Yahaya, *Int. J. Mol. Sci.* **2014**, *15*, 15044.

[54] a) F. Viela, D. Granados, A. Ayuso-Sacido, I. Rodríguez, *Adv. Funct. Mater.* **2016**, *26*, 5599; b) J. Vinje, K. S. Beckwith, P. Sikorski, *J. Microelectromech. Sys.* **2020**, *29*, 160.
[55] A. Huttenlocher, A. R. Horwitz, *Cold Spring Harb. Perspect. Biol.* **2011**, *3*, a005074.
[56] Y. Yang, K. Wang, X. Gu, K. W. Leong, *Engineering* **2017**, *3*, 36.
[57] M. Choi, S.H. Lee, W.B. Kim, V. Gujrati, D. Kim, J. Lee, J.-I. Kim, H. Kim, P.E. Saw, S. Jon, *Adv. Healthc. Mater.* **2016**, *5*, 101.
[58] E. Hebisch, M. Hjort, D. Volpati, C.N. Prinz, *Small* **2021**, *17*, 2006421.
[59] H. Steinle, A. Behring, C. Schlensak, H. P. Wendel, M. Avci-Adali, *Stem Cells* **2017**, *35*, 68.
[60] a) M. Huse, *Nat. Rev. Immunol.* **2017**, *17*, 679; b) P. Tolar, *Nat. Rev. Immunol.* **2017**, *17*, 621.
[61] a) V. Compan, A. Baroja-Mazo, G. López-Castejón, Ana I. Gomez, Carlos M. Martínez, D. Angosto, María T. Montero, Antonio S. Herranz, E. Bazán, D. Reimers, V. Mulero, P. Pelegrín, *Immunity* **2012**, *37*, 487; b) A. Upadhyaya, *Semin. Cell Dev. Biol.* **2017**, *71*, 137.
[62] D. Matsumoto, A. Yamagishi, M. Saito, R. R. Sathuluri, Y. R. Silberberg, F. Iwata, T. Kobayashi, C. Nakamura, *J. Biosci. Bioeng.* **2016**, *122*, 748.
[63] G. C. Messina, M. Dipalo, R. La Rocca, P. Zilio, V. Caprettini, R. Proietti Zaccaria, A. Toma, F. Tantussi, L. Berdondini, F. De Angelis, *Adv. Mater.* **2015**, *27*, 7145.
[64] A. Leis, Cellular Imaging Electron Tomography and Related Techniques in *Cellular Imaging Electron Tomography and Related Techniques*, (Eds: E. Hanssen), Springer, Cham, Switzerland **2018**, p1.
[65] S. Kumari, S. Mg, S. Mayor, *Cell Res.* **2010**, *20*, 256.
[66] a) J.-P. Grossier, G. Xouri, B. Goud, K. Schauer, *EMBO J.* **2014**, *33*, 35; b) T. Kawauchi, *Int. J. Mol. Sci.* **2012**, *13*, 4564.
[67] E. J. Ezratty, C. Bertaux, E. E. Marcantonio, G. G. Gundersen, *J. Cell Biol.* **2009**, *187*, 733.

Table of contents

Polymeric nanoneedles mediate stiffness-independent intracellular delivery

Hao Zhe Yoh,# Yaping Chen,# Stella Aslanoglou, Sherman Wong, Zlatan Trifunovic, Simon Crawford, Esther Lestrell, Craig Priest, Maria Alba, Helmut Thissen, Nicolas H. Voelcker,* Roey Elnathan**

H. Yoh, Dr. Y. Chen, S. Aslanoglou, E. Lestrell, Dr. M. Alba, Prof. N. H. Voelcker, Dr. R. Elnathan
Monash Institute of Pharmaceutical Sciences
Monash University
381 Royal Parade, Parkville, VIC 3052, Australia
E-mail: crystal.chen@monash.edu; nicolas.voelcker@monash.edu; roey.elnathan@monash.edu

H. Yoh, Dr. Y. Chen, S. Aslanoglou, E. Lestrell, Dr. M. Alba, Prof. N. H. Voelcker, Dr. R. Elnathan

Melbourne Centre for Nanofabrication
Victorian Node of the Australian National Fabrication Facility
151 Wellington Road, Clayton, VIC 3168, Australia

H. Yoh, E. Lestrell, Dr. M. Alba, Dr. H. Thissen, Prof. N. H. Voelcker
Commonwealth Scientific and Industrial Research Organisation (CSIRO)
Clayton, VIC 3168, Australia

Prof. N. H. Voelcker, Dr. R. Elnathan
Department of Materials Science and Engineering, Monash University, 22 Alliance Lane,
Clayton, VIC 3168, Australia.

Prof. N. H. Voelcker
INM-Leibnitz Institute for New Materials, Campus D2 2, Saarbrücken 66123, Germany.

A/Prof. C. Priest
Future Industries Institute, University of South Australia, Mawson Lakes, SA, 5095 Australia

A/Prof. C. Priest
Australian National Fabrication Facility, South Australia Node, Mawson Lakes, SA, 5095
Australia

Dr. S. Wong
Physics, School of Science, RMIT University, Melbourne, VIC 3000, Australia

Z. Trifunovic
Ian Holmes Imaging Centre
Bio21 Molecular Science and Biotechnology Institute
The University of Melbourne, VIC 3010, Australia

S. Crawford
Ramaciotti Centre for Cryo Electron Microscopy,
Monash University, VIC 3800, Australia

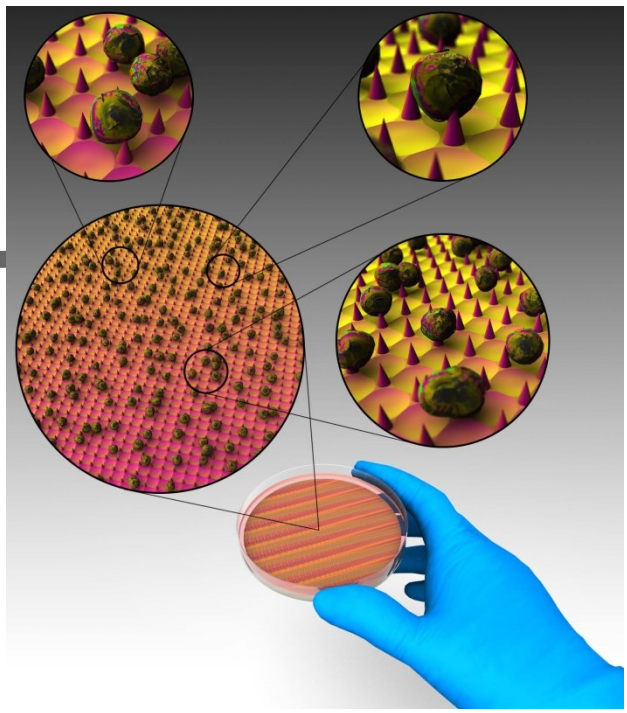

Figure 1: Integration of arrays of polymeric nanoneedles onto cell-culture Petri dish for effective and scalable intracellular gene delivery

Polymeric nanoneedle arrays of precise geometry, were fabricated using commercially available polymers—polystyrene, SU8, and polydimethylsiloxane—to facilitate mRNA delivery into both adherent and suspension mammalian cells. By comparing nanoneedle substrates of identical topography but varying stiffness, this study decoupled the effects on cell behavior of substrate stiffness and topography.